12. Wall-Bounded Flows

Turbulent wall-bounded flows (i. e., boundary layer, pipe and channel flows) present additional measurement challenges relative to those in, say, free shear turbulent flows or grid turbulence. The physical presence of the wall and the limitations and influences it presents on the implementation of sensing technologies creates some of these challenges. Other, often more-subtle issues, however, relate to the effect that the wall has on the inherent flow dynamics. Such effects are reflected in the steep mean velocity gradient(s) in the vicinity of the surface, as well as the length and time scales of the turbulence local to the near-wall region. Regarding the latter, primary challenges are associated with the high frequencies and small scales of near-wall turbulence relative to free shear flows.

In previous Chaps. (5.2, 5.3 and 5.5.3), relatively broad discussions were provided regarding the requirements and considerations for accurate measurements of both mean and fluctuating quantities in turbulent flows. The present chapter constitutes an extension of these more-generic considerations relative to the specific case of wall-bounded turbulent flows. For the purposes of providing a background context, the initial subsection below presents a brief overview of concepts and considerations specific to wall flows. Owing to its central role in the study of the turbulent wall flows, the next subsection addresses the measurement of the wall shear stress for ca-

Part C | 12

nonical boundary layer, pipe and channel flows. Considerations relative to transitional and non-canonical wall flows are presented in subsequent subsections.

12.1 Introductory Concepts

Prior to detailed discussions relative to specific measurement objectives, it is useful to provide a brief overview of background information relevant to the experimental study of wall-bounded turbulence.

12.1.1 Governing Equations

This subsection provides a brief presentation and discussion of the governing equations for the canonical

turbulent boundary layer, pipe, channel flows. In each case, the development will be for incompressible, constant property flows, governed by the Reynolds averaged Navier–Stokes (RANS) equations presented previously in Sect. 10.1, and for convenience repeated here in Cartesian form for a statistically stationary flow without body forces

$$\rho \left(U\frac{\partial U}{\partial x} + V\frac{\partial U}{\partial y} + W\frac{\partial U}{\partial z} + \frac{\partial \overline{u^2}}{\partial x} + \frac{\partial \overline{uv}}{\partial y} + \frac{\partial \overline{uw}}{\partial z} \right)$$
$$= -\frac{\partial P}{\partial x} + \mu \left(\frac{\partial^2 U}{\partial x^2} + \frac{\partial^2 U}{\partial y^2} + \frac{\partial^2 U}{\partial z^2} \right) , \qquad (12.1)$$

$$\rho \left(U\frac{\partial V}{\partial x} + V\frac{\partial V}{\partial y} + W\frac{\partial V}{\partial z} + \frac{\partial \overline{vu}}{\partial x} + \frac{\partial \overline{v^2}}{\partial y} + \frac{\partial \overline{vw}}{\partial z} \right)$$
$$= -\frac{\partial P}{\partial y} + \mu \left(\frac{\partial^2 V}{\partial x^2} + \frac{\partial^2 V}{\partial y^2} + \frac{\partial^2 V}{\partial z^2} \right) , \qquad (12.2)$$

$$\rho \left(U\frac{\partial W}{\partial x} + V\frac{\partial W}{\partial y} + W\frac{\partial W}{\partial z} + \frac{\partial \overline{wu}}{\partial x} + \frac{\partial \overline{wv}}{\partial y} + \frac{\partial \overline{w^2}}{\partial z} \right)$$
$$= -\frac{\partial P}{\partial z} + \mu \left(\frac{\partial^2 W}{\partial x^2} + \frac{\partial^2 W}{\partial y^2} + \frac{\partial^2 W}{\partial z^2} \right) , \qquad (12.3)$$

$$\frac{\partial U}{\partial x} + \frac{\partial V}{\partial y} + \frac{\partial W}{\partial z} = 0 . \qquad (12.4)$$

In the above equations U, V and W are the mean velocity components in the x, y and z directions, u, v and w are the corresponding fluctuating velocity components, an overbar represents time averaging, ρ is the mass density and μ is the dynamic viscosity. Further discussion of the developments leading to (12.1), (12.2), (12.3) and (12.4) is given in Sect. 10.1.1.

Flat–Plate Boundary Layer

Two-dimensional boundary layer flow in the (x, y) plane is considered. The flow is generated by a constant free stream velocity, U_∞, flowing over a smooth flat plate located in the $y = 0$ plane of semi-infinite extent $(x \geq 0)$. As is conventional the boundary layer thickness, $\delta = \delta(x)$, is taken to be the y position where $U(y) = 0.99 U_\infty$. Under these constraints and to the leading order of boundary layer approximations [12.1–3] the RANS equations reduce to,

$$\rho \left(U\frac{\partial U}{\partial x} + V\frac{\partial U}{\partial y} + \frac{\partial \overline{uv}}{\partial y} \right) = \mu \frac{\partial^2 U}{\partial y^2} , \qquad (12.5)$$

$$\rho \frac{\partial \overline{v^2}}{\partial y} = -\frac{\partial P}{\partial y} , \qquad (12.6)$$

$$\frac{\partial U}{\partial x} + \frac{\partial V}{\partial y} = 0 . \qquad (12.7)$$

Equation (12.5) indicates that the time rate of change of mean axial momentum is determined by the sum of the viscous and Reynolds stress gradients. Unlike the laminar case, (12.6) indicates that the wall normal pressure gradient is nonzero, and is determined by the gradient of the Reynolds normal stress, $\overline{v^2}$. With regard to (12.5), it is also relevant to note that additional streamwise gradient terms of the axial and wall normal velocity variances can be significant, especially under adverse pressure gradient conditions [12.2].

Fully Developed Channel and Pipe Flows

Fluid-dynamically fully developed flow in the (x, y) plane between horizontal, effectively infinite, parallel plates is considered. Flow in the x direction is generated by a constant pressure gradient, $\mathrm{d}P/\mathrm{d}x < 0$. The lower plate is located at $y = 0$, and the spacing between the plates is 2δ. Under these constraints, all of the terms in (12.4) are identically zero and the mean differential force balance equations for the axial and wall-normal components reduce to (e.g., [12.1–3]),

$$\rho \frac{\mathrm{d}\overline{uv}}{\mathrm{d}y} = -\frac{\mathrm{d}P}{\mathrm{d}x} + \mu \frac{\mathrm{d}^2 U}{\mathrm{d}y^2} , \qquad (12.8)$$

$$\rho \frac{\mathrm{d}\overline{v^2}}{\mathrm{d}y} = -\frac{\mathrm{d}P}{\mathrm{d}y} . \qquad (12.9)$$

Under transformation from a cylindrical to a Cartesian coordinate system, (12.8) and (12.9) can also be shown to hold for fully developed flow in a pipe [12.2]. (A particularly thorough derivation of this is also given in the dissertation by *Sahay* [12.4].) In this case, the origin is transferred from the pipe centerline to the wall, and the pipe radius R corresponds to δ. Similar to the boundary layer equations, the axial mean flow in pipes and channels is governed by a three term equation, with the mean advection term being replaced by the mean pressure gradient in the case of pipes and channels. In all cases, the wall-normal pressure gradient is determined by the wall-normal gradient of the vertical velocity variance.

12.1.2 Brief Overview of Wall Flow Structure

Physical models of the mean structure of turbulent wall flows have emerged from the extensive body of research conducted over the past century. In what follows, two views of wall flow structure are briefly presented. Broadly speaking, the first comes about from consideration of the observed properties of the mean axial velocity profile, in concert with interpretations derived from observations of the relative magnitudes of the Reynolds
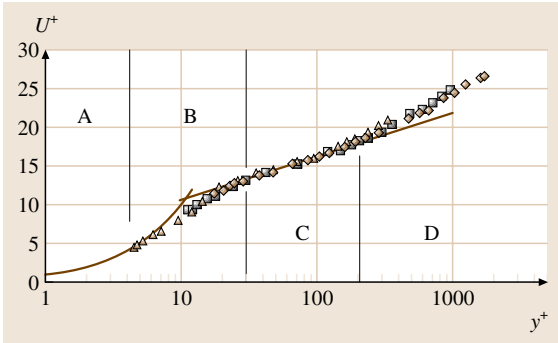
Fig. 12.1 Inner-normalized mean profiles in turbulent boundary layers and the associated layer structure: (A) viscous sublayer; (B) buffer layer; (C) logarithmic layer; (D) wake layer (Data from [12.5])
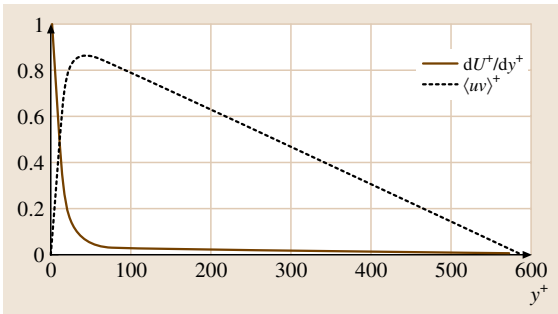

Fig. 12.2 Inner-normalized mean viscous and Reynolds shear stress profiles in turbulent channel flow $\delta^+ = 590$. (Data from [12.6])

and viscous stresses appearing in (12.5) and (12.8). The second, more recently developed interpretation, comes about by directly considering the relative magnitudes of the terms in these equations.

The prevalent view of the mean structure of turbulent wall flows [12.2, 3, 8] is largely derived from the observed properties of the mean velocity profile, along with the relative behaviors of the viscous and Reynolds stresses. Regarding the former, Fig. 12.1 shows characteristic turbulent boundary layer mean velocity profile data. In this figure the profiles have been made nondimensional using the so-called inner variables, u_τ and ν, where $u_\tau = \sqrt{\overline{\tau}_w/\rho}$ is termed the friction velocity, and ν is the kinematic viscosity. The predominant shorthand convention denotes inner variables with a superscript plus. Thus, the inner normalized wall-normal distance is denoted $y^+ = yu_\tau/\nu$. Regarding the latter, Fig. 12.2 reveals the relative magnitudes of the viscous and Reynolds stresses in turbulent channel flow. These

data reveal that the magnitude of $\overline{uv}^+$ is zero at the wall, but rapidly rises to a value that is $O(1)$ by $y^+ \simeq 30$. Conversely, dU^+/dy^+ equals 1.0 at $y^+ = 0$, but diminishes to a quantity much less than $O(1)$ by $y^+ \simeq 30$. Behaviors such as these have led to the four-layer structure depicted in Fig. 12.1 and are connected to the features of the mean profile. As indicated, the viscous sublayer (layer A) extends to about $y^+ = 5$, the buffer layer (B) nominally resides between $5 < y^+ < 30$, the logarithmic layer (C) extends from near $y^+ = 30$ to $y/\delta \simeq 0.2$, and the wake layer (D) extends from the outer edge of the logarithmic layer to the outer edge of the boundary layer, $0.2 \leq y/\delta \leq 1$.

An alternative layer structure [12.7] may be derived through consideration of the relative magnitudes of the terms in the mean momentum equation. In this case, the layer structure directly reflects the dominant dynamical effects according to the mean differential statement of Newton's second law. One way to reveal this layer structure is by examining the ratio of the viscous stress gradient to Reynolds stress gradient terms in (12.5) and (12.8). Figure 12.3 schematically depicts the resulting layer structure at a fixed Reynolds number. The layer closest to the wall (layer I) is characterized by a nominal balance between mean advection and the viscous stress gradient (pressure gradient and viscous stress gradient in a pipe or channel). To a very good approximation, the adjacent layer (II) is represented by a balance between the Reynolds stress gradient (turbulent inertia) and viscous stress gradient. Across layer III (except-
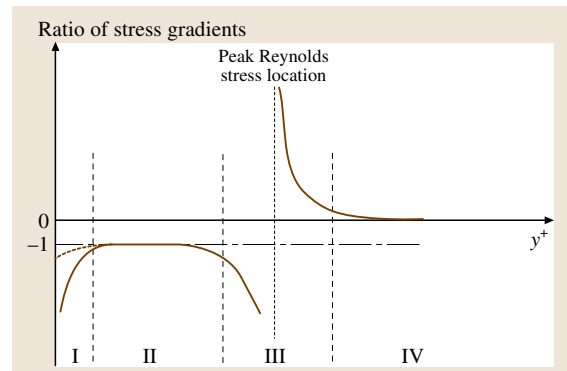

Fig. 12.3 Schematic of the structure of the boundary layer as derived from consideration of the mean momentum balance: (I) viscous stress gradient/mean advection balance layer; (II) viscous/Reynolds stress gradient balance layer; (III) Reynolds stress gradient/viscous stress gradient/mean advection balance layer; (IV) Reynolds stress gradient/mean advection balance layer (after [12.7])

ing in the immediate vicinity of the peak position of the Reynolds stress) all three terms in the mean momentum balance are of the same order, while in layer IV the mean dynamics are well represented by a balance between the Reynolds stress gradient and mean advection (or pressure gradient in a channel). The inner normalized layer widths depicted in Fig. 12.3 scale differently with Reynolds number, say $\delta^+ = u_\tau \delta / \nu$, than those in Fig. 12.1. For example, from the layer structure of Fig. 12.3 one surmises that the mean effect of viscous forces remains of dominant order much farther from the wall than indicated by the layer structure of Fig. 12.1.

12.1.3 Scaling Ideas and Parameters

Under either layer structure presented above, it is apparent that the variation of turbulent wall flow behavior with Reynolds number is characterized by a variety of scaling parameters. Relative to the theory associated with the layer structure depicted in Fig. 12.1 two independent sets of scales are required: the so-called inner and outer scales. Relative to the theory associated with the layer structure depicted in Fig. 12.3, there are three interdependent scales. In this case given any two the third may be derived. As introduced above, inner scales (e.g., length, time, velocity) are dimensionally constructed using the friction velocity and kinematic viscosity u_τ and ν, respectively. Similarly, outer scaled variables are constructed using a measure of the overall layer thickness, i.e., δ, δ^* or θ (disturbance, displacement and momentum-deficit thicknesses, respectively [12.9]), and the free stream velocity U_∞ or the deviation from the free stream velocity, $(U_\infty - U)$. (Note that in a channel flow, the maximum velocity replaces U_∞.) Nominally, the inner scales are appropriate for the characterization of the flow physics near the surface. Alternatively, outer parameters are appropriate for scaling the bulk or large scale properties of the motion centered away from the wall. In connection with this, a primary attribute of any theory of wall turbulence involves describing, as a function of Reynolds number, how the inner scaling behaviors near the wall merge with the outer scalings appropriate away from the wall. Under the theory relating to the layer structure of Fig. 12.1, this occurs in the logarithmic (or overlap) layer, where there is hypothesized to be joint validity of inner and outer scaling [12.2, 3, 8]. In the alternate view, the merging process occurs via a hierarchy of self-similar layers whose wall-normal extent asymptotically scales with the distance from the wall [12.10]. As elucidated further below, however, the physical significance of the scaling parameters are not only relevant to theoretical formulations, but are of central importance when considering the rational design of experiments.

12.1.4 Overview of Measurement Considerations

A number of important factors are worthy of careful consideration when planning for experiments of boundary layer turbulence, and particularly those in the immediate vicinity of the wall. These relate to the dynamically relevant length and time scales of the flow, the potential influences of the high mean shear near the wall on the efficacy of the measurement technique, as well as potentially detrimental effects of the wall itself on the measurement technology being employed. In addition, the convergence criteria for near-wall turbulence statistics are generally much more stringent than those in free shear flows.

Temporal and Spatial Resolution
Under general discussions of spatial and temporal resolution requirements for turbulent flow (Sect. 5.2) the length and time scales associated with Kolmogoroff scale ($\eta = (\nu^3/\epsilon)^{1/4}$, where ϵ is the mean turbulence dissipation rate) provide useful criteria relative to the size and frequency of smallest dynamical motions. That is, η itself is a measure of the smallest eddy, and for such an eddy advecting at mean velocity U an estimate of its associated circular frequency is given by $f_K = U/(2\pi\eta)$. In wall turbulence, a similar set of notions holds, but in this case the inner length scale, ν/u_τ, is typically employed as a measure of the smallest turbulent mo-
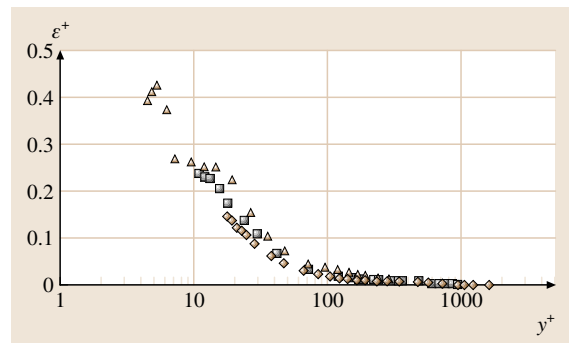

Fig. 12.4 Inner normalized profiles of the turbulence dissipation rate in zero-pressure-gradient turbulent boundary layers. In these profiles ϵ was estimated using an approximate formula based on the measurement of five velocity gradient variances [12.5]

tions. As revealed by the estimates given in Fig. 12.4, the Kolmogoroff scale is larger than the viscous scale, and depending on the distance from the wall, it can be considerably larger. Also note that u_τ^2/ν does not provide a good estimate for the highest frequency in the flow, say, for determining sampling rate. That is, while it is an inner frequency (equalling $\partial U/\partial y|_{\text{wall}}$), and does not account for the higher effective frequency associated with the advection of $O(\nu/u_\tau)$-scale eddies.

Sensor spatial resolution has proven to play a particularly important role in the study of wall turbulence, since, for example, relatively subtle Reynolds number dependencies can be masked by the competing counter-influence of decreasing spatial resolution with increasing U_∞. (Note that it is often most convenient to increase U_∞ to increase R_θ.) Important studies that have specifically examined single wire sensor resolution issues in wall-bounded flows include those by *Johansson* and *Alfredsson* [12.11], *Ligrani* and *Bradshaw* [12.12] and *Klewicki* and *Falco* [12.5]. In their study of turbulent channel flow, Johansson and Alfredssson showed considerable attenuation ($\simeq 15\%$) in the peak value of the axial intensity for nondimensional sensor lengths ranging from $4 \leq \ell^+ \leq 32$. They also concluded that the attenuation effect is large relative to Reynolds number dependence. In their sub-miniature hot-wire-based study of viscous sublayer turbulence in boundary layers Ligrani and Bradshaw showed very similar attenuation as in the study of Johansson and Alfredsson, and concluded that sensors having an ℓ^+ less than about 20 should be sufficient for capturing wall layer axial velocity statistics. From the analysis of a compilation of existing high resolution data and their own high-resolution boundary layer measurements, *Klewicki* and *Falco* [12.5] conclude that the peak axial velocity intensity begins to attenuate when the sensor length exceeds about eight viscous units, and that the Reynolds number dependence is smaller, but not necessarily small, in comparison with the attenuation effect. The more-recent high-resolution laser-Doppler anemometer (LDA) measurements of *DeGraaff* and *Eaton* [12.13] support these

findings. Overall, relative to axial velocity statistics a common *rule of thumb* suggestion is that the characteristic sensor dimension be less than about a fifth of the distance from the wall. This is viewed as constituting a reasonable, albeit rigorously unproven, criterion.

The situation becomes more complex when considering the spatial resolution requirements for the wall normal velocity component or velocity gradients and vorticity components. For x-array hot-wire probes, effects relating to both the wire length and wire spacing must be considered, as well as whether there is a significant shear across the array [12.14]. In the case of velocity gradients and vorticity components, in principle, the objective is to attain a sensing dimension comparable to the Kolmogoroff microscale (or equivalently a small number of viscous units). In practice, however, this objective must be weighed against the effect of noise contained in signals derived from sensors that are positioned very close to each other [12.5, 15]. Regarding this issue, the results by *Folz* [12.16] based upon experiments in the atmospheric surface layer (a very high Reynolds number boundary layer) indicate that hot-wire spacings in the range of $2\pi\eta$ are optimal with regard to resolving the instantaneous gradients in the logarithmic layer.

Lastly, there are a number of measurement issues that become significant for sensors positioned in the immediate vicinity of the surface. For physical probes (e.g., Pitot tubes and hot-wire sensors) aerodynamic blockage and localized flow accelerations can become significant as the probe nears the surface [12.17]. Conduction heat transfer from a hot-wire probe to the wall is also a well-documented phenomenon, although this can be mitigated to some extent by the choosing a non-conductive surface and/or reducing the heating ratio of the wire. For optical techniques (e.g., LDV and PIV) maintaining sufficient particle seeding can pose significant challenges in the vicinity of the surface. These techniques can be influenced by unwanted light reflections from the surface as well [12.18, 19]. For LDV, the strong mean shear in and near the viscous sublayer can also cause biased measurements (Sect. 5.3.1).

12.2 Measurement of Wall Shear Stress

The wall shear stress is of central importance for both theoretical and practical reasons. When viewed as a *dynamical machine*, the primary mechanism of the turbulent boundary layer relates to its capacity to convert free-stream momentum into a shear force acting over

the surface. Indeed, when viewed in this way the skin friction coefficient,

$$C_\text{f} = \frac{\overline{\tau}_\text{w}}{\frac{1}{2}\rho U_\infty^2} \ , \tag{12.10}$$

is a measure of this capacity (per unit surface area) as it constitutes the ratio of the mean wall shear stress to the axial free-stream momentum flux per unit area. Of course, from the perspective of engineering applications the accurate prediction of C_f, say as a function of R_θ, is required for the design of streamlined vehicles (e.g., aircraft and submarines) over their operating velocity ranges. Similarly, the considerations briefly outlined in Sect. 12.1.2 reveal that $\overline{\tau}_w$ (often through u_τ) constitutes a primary scaling parameter relative to theoretical treatments of wall turbulence. Lastly, the fluctuating wall shear stress has fundamental importance to the basic physics of wall-bounded flows, having, for example, relevance to improved methods for flow management and control, as well as numerical predictive methods such as large eddy simulation.

In what follows, a number of techniques for measuring the wall shear stress are discussed, and some of the key references are given for each technique. These discussions will focus on the underlying measurement principles along with the primary considerations relating to the appropriateness and application of each technique in the context of specific measurement objectives. As mentioned at the beginning of this section, many of the challenges in wall-bounded flows center on the rather stringent spatial and temporal resolution requirements for accurate near-wall measurements.

12.2.1 Methods for Determining the Time-Averaged Wall Shear Stress

Wall-flow experimental designs should carefully consider what type of wall shear stress information is required to meet the experiment objectives. That is, general techniques designed to give the spatially and temporally resolved wall shear stress can certainly also be used to obtain the time mean value. Such techniques, however, must obtain estimates of the instantaneous differential force acting over a differential area of the surface (rather than an estimate of the average force acting over a finite area), and thus their accuracy relative to estimating the mean is often diminished. It is for this reason that in cases where only the mean is required, techniques designed for this specific objective are generally preferred.

Methods Involving Measurements at the Surface

Oil film interferometry (OFI) and two pressure-based methods are considered. OFI relies on the measurement of the optically produced fringe pattern associated with

light reflections from a thin film of oil on the surface over which there is a wall flow. Thus, this technique requires optical access to the facility test section. The first of the pressure-based techniques relies on the relationship between the axial mean static surface pressure variation in a duct, and its validity is restricted to the condition of fully developed flow. The second pressure-based technique, the Preston tube method, constructs a correlation between the stagnation pressure produced by the velocity profile near the surface, and thus implicitly relies on the inner-normalized universality of the mean profile over a region of the flow near the wall.

Oil–Film Interferometry. *Tanner* and *Blows* [12.20] were the first to utilize Fizeau interferometry to measure the thinning rate of an oil film deposited on a surface and subjected to a bounding flow. The basis of the technique stems from the analytical solution for flows at very low Reynolds number within the oil film. As fluid flows over the test surface, the oil film begins to thin owing to the action of the surface shear stress imparted by the bounding flow. During this thinning processes, and through the use of interferometry, the spatially and temporally varying thickness of the oil film is determined. Once the film thinning rate is known, the mean wall shear stress can be evaluated using a form of the thin-oil-film equation (12.13). Since oil film thicknesses can be measured using relatively inexpensive and simple equipment, this is often an attractive method for measuring the mean wall shear stress [12.21]. As apparent from its underlying principle, the oil-film interferometry method is restricted to smooth wall flows. In this context it is relevant to note that typical oil thicknesses are on the order of a micron, and thus for a very large number of flow
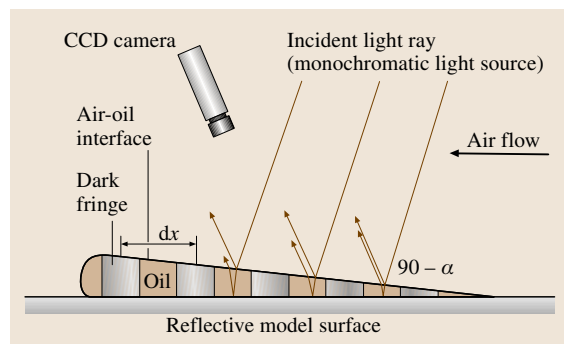

Fig. 12.5 Schematic of a typical oil-film interferometry setup (not to scale). Note that the observer viewing angle α is the deviation from normal to the surface

situations the distortion of the surface caused by the oil itself is negligible.

As indicated by the schematic of Fig. 12.5 the necessary equipment for the oil-film technique typically includes a monochromatic light source, appropriate test surface, oil film and detector (e.g., a CCD camera). While the equipment utilized by this method is fairly uncomplicated, some equipment selections will produce better images than others. Specifically, a non-laser light source such as a sodium lamp is suitable for these measurements and is actually preferable to laser light [12.21]. Additionally, *Zilliac* [12.23] has tested several surface materials and reports that polished aluminum produces poor fringes whereas polished stainless steel, mylar film, and SF 11 glass (among others) all produce satisfactory fringes. Finally, oil with a viscosity that changes little with temperature is favored since sensitivity to changes in temperature can be a source of significant measurement error [12.23]. Silicone oils are especially attractive in this regard.

In order to calculate the mean wall shear stress, the thickness of the oil film is determined using Fizeau interferometry. When a monochromatic light source illuminates the surface of a thin film, a portion of the incident light is reflected off of the oil surface while the residual portion travels through the thin film and reflects off of the surface of the test piece. As shown in Fig. 12.6, when the reflected light is collected, a series of light and dark bands appear as a result of constructive or destructive interference, depending upon the oil height at a particular position. The film thickness at the k-th (dark) fringe is given as,

$$h_k = h_0 + k\Delta h \,, \quad k = 0, 1, 2, \dots , \tag{12.11}$$

where h_0 is the oil height at the zeroth fringe and the difference in height between successive fringes is given by

$$\Delta h = \frac{\lambda}{2(n^2 - \sin^2 \alpha)^{1/2}} \,. \tag{12.12}$$

Here, λ is the wavelength of the light source, n is the refractive index of the oil and α is the observer viewing angle. Minimizing the observer viewing angle, α, to the smallest possible values generally produces the highest-contrast fringe pattern. An example of a series of oil-film fringes, taken at various times, is shown in Fig. 12.6.

According to *Tanner* and *Blows* [12.20], the motion of the oil film is influenced by shear stress, pressure gradients, gravity, oil surface curvature and surface tension. With the aid of dimensional analysis, however, it has been shown [12.24] that for a sufficiently thin film,
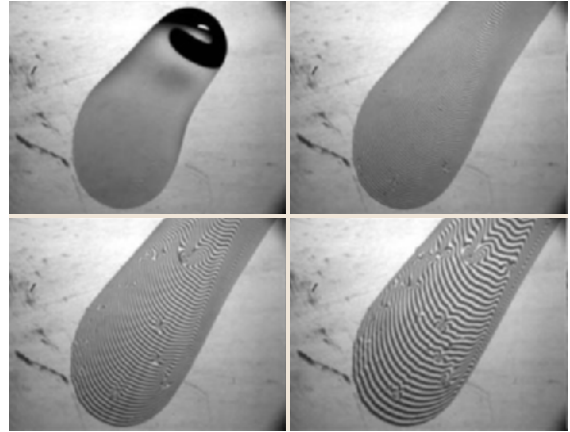

Fig. 12.6 Example fringe patterns as derived from oil film light reflections (after [12.22]). Flow is from the *upper right*

the motion of the oil is primarily due to the action of shear stress on its surface. Therefore, in most cases, the thin-oil-film equation for a two-dimensional flow reduces to

$$\frac{\partial h}{\partial t} = -\frac{1}{2\mu} \frac{\partial(\overline{\tau}_w h^2)}{\partial x} \,. \tag{12.13}$$

Under conditions where the shear stress is not the only dominant force influencing the motion of the oil, or if the flow is three dimensional, a more general form of the thin-oil-film equation should be used [12.21, 24].

Several methods have been developed to calculate the average wall shear stress using (12.13), and these are reviewed by *Naughton* and *Sheplak* [12.21] and *Fernholz* et al. [12.25]. Fernholz et al. derive two particularly simple methods from (12.13) under the assumption that the wall shear stress is constant. The first method is given by,

$$\overline{\tau}_w = \frac{\mu x}{ht} \,, \tag{12.14}$$

while the second is expressed as,

$$\overline{\tau}_w = \mu u_k \frac{2(n^2 - \sin^2 \alpha)^{1/2}}{\lambda(k + h_0/\Delta h)} \,, \tag{12.15}$$

where

$$u_k = \frac{\partial x}{\partial t}\Big|_{h_k = \text{const}} \,. \tag{12.16}$$

While the second method appears to be more difficult to implement than the first because of the need to determine u_k (the fringe velocity), the form of the first may be deceptively simple since the height of the zeroth fringe

(h_0) must also be measured in order to calculate the height of the oil at a given location [12.26]. In the second method, however, measurements can be made that allow h_0 to be calculated from a single data set using multiple fringes [12.25]. That is, in (12.15) n, μ, α and λ are known, and u_k can be calculated from (12.16) using images of the fringe pattern taken at known times after the $u_k =$ constant condition has been attained. Automated image-processing methodologies for determining the fringe spacing are relatively easy to implement. These generally involve finding either the leading or trailing edge of the fringe (edge detection-based method) or locating the fringe center (peak grayscale intensity-based method). Multiple fringe spacing estimates from each image can be used to construct statistically robust measurements.

While both of the above methods are based on the assumption of constant mean shear stress, errors should not be large if these methods are applied to flows with moderately varying $\overline{\tau}_w$ provided that,

$$\frac{\Delta \overline{\tau}_w}{\overline{\tau}_w} \ll \frac{\partial h}{\partial x} \tag{12.17}$$

in the vicinity of the measurement location. It is important to check that this relation holds when using these methods since large errors may otherwise result [12.24]. Although the cases considered here are for time-invariant wall shear stress, several methods have been developed for cases where the shear stress is time dependent [12.25]. Additionally, solution methodologies exist for three-dimensional flows [12.21].

Some of the error sources and difficulties associated with this method include dust, humidity, high-shear situations, oil property variations, oil evaporation, shear stress variation, surface tension, pressure gradients and gravity effects. Fringe pattern degradation due to dust and humidity may be prevented by eliminating both from the test environment. Undesirable surface waves, that sometimes form under high-shear conditions, may also be avoided if the oil film is initially very thin [12.27]. Oil property variations may become a significant source of error and should be monitored throughout a test. Also, oil evaporation may cause the film to appear to thin faster than it actually does – this problem may be avoided by using oils having a low vapor pressure, e.g., silicone oils [12.28]. Finally, effects due to shear stress variation, surface tension, pressure gradients and gravity may be accommodated via selection of the appropriate form of the thin-oil-film equation [12.21, 24].

Mean Pressure–Gradient Method. A simple, yet highly accurate, method for measuring the average wall shear stress is available for fully developed internal flows. When the flow satisfies the conditions of being fully developed and two-dimensional (planar or axisymmetric) the mean wall shear stress $\overline{\tau}_w$ may be calculated from the measured axial pressure gradient. As elucidated in many undergraduate fluid-mechanics textbooks [12.9], a control volume analysis of a fully developed pipe or channel flow of constant cross-sectional area A_c reveals that the mean pressure drop ΔP present over a length L of the duct is related to the average wall shear stress acting over the surface area A by

$$\Delta P A_c = \int_A \overline{\tau}_w \, dA \ . \tag{12.18}$$

For fully developed flow the surface shear stress per unit length of the duct is constant. Thus for a circular pipe

$$\overline{\tau}_w = \frac{\Delta P}{2L} \delta \tag{12.19}$$

and in a two-dimensional channel,

$$\overline{\tau}_w = \frac{\Delta P}{L} \delta \ , \tag{12.20}$$

where δ is either the pipe radius or channel half-height, respectively.

Harotinidis [12.29] asserts that this momentum-balance-based method is perhaps the most reliable for flows that satisfy the requisite flow conditions. Unfortunately, the applicability of this method is operationally quite limited since, in practice, it is not a trivial matter to exactly attain both the fully developed and two dimensional (axisymmetric) conditions. For example, recent results by *Lien* et al. [12.30] reveal that even in channel flows of aspect ratio greater than 12, the apparent effect of the side walls is felt in the core flow. Indeed, one may construct a physically rational argument that flow in a circular pipe is the only for which the fully developed and axisymmetric (two-dimensional) conditions can be attained to the same degree as prescribed mathematically. That is, any real channel will be finite in its span, and the side wall boundary layers will, in all likelihood, continue to grow with downstream distance. Contrary to this physical argument, *White* [12.31] provides an analysis supporting the notion that after sufficient development length the growth of the side wall boundary layers is, in fact, arrested. Interestingly, studies exploring laminar to turbulent transition cite the need for exceptionally long development lengths ($\simeq 400$ channel heights, 2δ) and especially wide channels (≥ 27 channel

heights) [12.32], while high-quality turbulent flow studies are generally in the range of about 200δ and greater than 20δ for the development length and channel width, respectively. Overall, it is recommended that channel flow studies carefully verify a fully developed condition prior to utilizing the pressure drop for determining the wall shear stress.

Of course, even for fully developed pipe flow, experimental details relating to the accurate measurement of static pressure must be carefully considered. Such effects include the finite size of the pressure taps (which tends to cause an overestimation of the true pressure), as well as the quality of the tap hole relative to the internal surface of the pipe. Particularly important references in this regard include the studies of *Shaw* [12.33], *Franklin* and *Wallace* [12.34], *Ducruet* and *Dyment* [12.35], *McKeon* and *Smits* [12.36], as well as Sect. 5.1 in this handbook. Careful consideration of these effects can minimize the associated uncertainty in $\overline{\tau}_w$ to a small fraction of a percent [12.37]. Lastly, it is not advisable to use this method for flows that do not satisfy the assumptions underlying (12.19), since significant and difficult to characterize errors are likely to result [12.38].

Preston Tube Method. Though not a measurement acquired precisely at the wall, the method initially developed by *Preston* [12.39] utilizes stagnation pressure information derived from a tube placed on the wall. In some sense, this method can be considered a *single point* variant of the Clauser plot technique described below. This is because it relies on the correlation between $\overline{\tau}_w$ and the difference between the surface static pressure and the stagnation pressure produced by the portion of the mean velocity profile in the region of the flow where the so-called *law of the wall* is valid. The dimensional analysis underlying this arrives at the correlating expression

$$\frac{\overline{\Delta P}}{\overline{\tau}_w} = f\left(\frac{\mathrm{d}^2 \overline{\tau}_w}{\rho \nu^2}\right) , \qquad (12.21)$$

where $\overline{\Delta P}$ is the mean difference between the pressure sensed by the stagnation (Preston) tube and the static pressure obtained from a nearby wall tap, and d is the outside diameter of the tube.

In any given flow, the wall thickness of the tube determines which portion of the mean profile contributes to the stagnation pressure sensed at the tube opening. For relatively thick turbulent wall flows and very small tubes, the measurement could be fully immersed in the viscous sublayer. In this case, the mean profile existing across the tube opening will be linear. Under most

measurement situations, however, the finite wall thickness of a typical tube will result in the location of the tube opening being primarily in the logarithmic portion of the mean profile. It is for this situation that the majority of Preston tube calibrations have been developed. Popular among these are the calibration equations given by *Patel* [12.40], as well as the tabulated calibration given by *Head* and *Ram* [12.41] (also see *Hanratty* and *Campbell* [12.42]). Owing to the accuracy by which the mean wall shear stress can be independently determined, fully developed pipe flows have traditionally been the flow field of choice for calibrating Preston tubes.

While the Preston tube method is a simple (albeit correlation-based) technique for estimating $\overline{\tau}_w$, its limitations should be understood and some care must be taken in its implementation. Except under the condition where the tube opening is fully contained in the viscous sublayer, an important assumption implicit to the technique is that a logarithmic *law-of-the-wall* region exists in the flow considered, and that the tube opening resides in and/or below this portion of the profile. Thus, the technique is inappropriate for highly nonequilibrium wall flows, or other situations where the logarithmic portion of the mean profile has been significantly altered. This said, *Patel* [12.40] does provide some recommendations pertaining to the use of Preston tubes in boundary layer flows with axial pressure gradients. Furthermore, existing smooth wall calibrations should not be applied under rough wall situations. On the other hand, while Preston indicated that the ratio of the inner to outer diameter of the tube is important, the later study by Patel showed little sensitivity to this parameter as long as the ratio is greater than 0.2. Alignment of the Preston tube in the flow direction can be a significant source of error, especially in three dimensional boundary layers where the mean flow direction is not always easy to determine and instantaneous nonlinear yaw effects affect the measured mean value. Consistent with the behavior of Pitot tubes, errors in $\overline{\tau}_w$ of about 1% are realized for a misalignment of about 3°. Lastly, care must be taken to make certain that the flow at the surface static pressure port is not influenced by the presence of the Preston tube on the wall.

Mean–Profile–Based Methods

Three different methods for determining the time-averaged shear stress from mean velocity profile data are considered. The von Karman integral method relies on the computation of the displacement and momentum deficit thicknesses, and thus requires measurements of

the mean velocity profile. This technique is restricted to two-dimensional flows, and under some circumstances the accuracy is diminished without the measurement of streamwise gradient terms of the velocity variances. The so-called Clauser plot method is an indirect technique that relies on the observed correlation between the wall shear stress and the properties of the logarithmic mean velocity profile characteristic of wall bounded flows (Fig. 12.1). Implicit in this technique is the assumption of a universal logarithmic mean velocity profile. The mean wall gradient method involves accurately measuring the linear portion of the mean velocity profile in the immediate vicinity of the surface. This technique, however, can only be utilized in flows over smooth walls.

von Karman Momentum Integral Method. For two-dimensional developing flows, the surface stress is related to the momentum and displacement thickness by von Karman's momentum integral equation. For flows where the streamwise variation in the fluctuating velocity variances are not large, the relationship between shear stress and the properties of the mean profile is given by [12.31]

$$\frac{\overline{\tau}_w}{\rho U_\infty^2} = \frac{d\theta}{dx} + (H+2)\frac{\theta}{U_\infty}\frac{dU_\infty}{dx} . \qquad (12.22)$$

Here, $H = \delta^*/\theta$ is the shape factor. Equation (12.22) includes the effects of axial pressure gradient, and thus for flat-plate boundary layer flow the last term is zero. When streamwise variations in the turbulence are non-negligible a more-complicated equation is required, and is given by [12.2]

$$\frac{\overline{\tau}_w}{\rho U_\infty^2} = \frac{d\theta}{dx} + (H+2)\frac{\theta}{U_\infty}\frac{dU_\infty}{dx}$$
$$- \frac{1}{U_\infty^2}\int_0^\delta \frac{\partial}{\partial x}(\overline{u^2} - \overline{v^2})\,dy$$
$$+ \text{higher-order terms} . \qquad (12.23)$$

Unlike the mean pressure gradient method in ducts, the momentum integral approach does not require that the flow be fully developed. Similar to the pressure-gradient method, however, its usefulness is often diminished by the practical difficulties associated with employing it. For example, under all cases considerable care must be taken to ensure that the flow under investigation is indeed adequately planar. Additional difficulties associated with this method can also arise, in part, from the need for accurate measurements of axial velocity gradients and in some cases axial gradients of the velocity variances. In specific reference to this last point,

recent experimental evidence [12.43, 44] indicates that even under the condition of zero pressure gradient the streamwise velocity variance gradients contribute about 5% to the overall integral momentum balance.

Clauser Plot Method. *Clauser* [12.45] observed that the wall shear stress in turbulent boundary layers could, under equilibrium conditions, be estimated with reasonable accuracy through its correlation with the law of the wall. Equilibrium flows are those whose statistical profiles can be represented (or nearly represented) in a self-preserving form using locally determined integral parameters. Accordingly, Clauser's observation forms the basis for the method that bears his name. Essentially, the Clauser plot is a graphical method for determining wall shear stress using the properties of the time-averaged velocity profile in the logarithmic portion of the boundary layer. The attractive feature of this method is that velocity measurements in the viscous sublayer portion of the profile, that are often difficult to obtain, are not required. Conversely, however, deviations from canonical behavior may preclude the use of this method. Indeed, recent experiments strongly support the assertion that for the purposes of discerning detailed mean profile scaling behaviors an independent means of obtaining the wall shear stress is required [12.46]. Hence, this method can only be recommended for those cases where a nominally accurate $\overline{\tau}_w$ value is acceptable.

In inner normalized form, the logarithmic equation for the mean profile is given by,

$$\frac{U}{u_\tau} = \frac{1}{\kappa}\ln\left(\frac{yu_\tau}{\nu}\right) + B , \qquad (12.24)$$

where, as indicated previously, the friction velocity u_τ is given by

$$u_\tau = \sqrt{\frac{\tau_w}{\rho}} , \qquad (12.25)$$

and, according to the logarithmic law assumptions, κ (the von Karman constant) and B are constants. Perhaps the most often cited values for κ and B are 0.41 and 5.0, respectively [12.47], although other values are often used as well. Using equation (12.24) and the fact that the skin friction coefficient can be expressed as $C_f = 2(u_\tau/U_\infty)^2$, allows the construction of the Clauser plot. In particular, when U/U_∞ is plotted versus $U_\infty y/\nu$ a series logarithmically varying lines are generated, with each line corresponding to a specific value of C_f. Thus, as depicted in Fig. 12.7, when measured mean velocity profile data are overlaid on this graph, the wall shear stress estimate is obtained according to the best
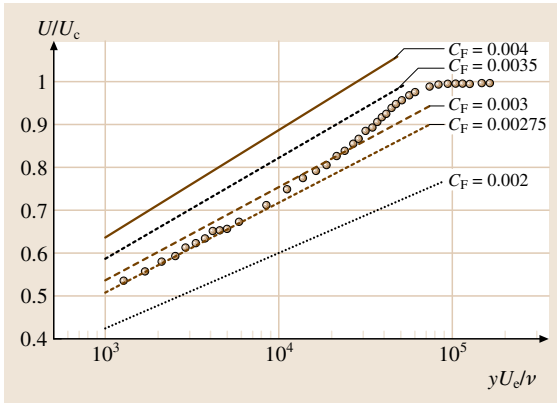
Fig. 12.7 Clauser plot with data [12.48]. Note that in the axis label U_e is used to denote the free-stream velocity

correspondence between the logarithmic portion of the velocity data and one of the parametric C_f lines.

The Clauser method is capable of producing reasonably accurate results, say $\pm 5\%$. It is worth emphasizing, however, that the sole basis of this method relies on the existence and validity of the logarithmic law. Given this, the Clauser plot method should be viewed as a useful means of approximating the value of the friction velocity, but it is neither a direct nor independent method. For example, this method is clearly not appropriate for use under conditions where a well-defined logarithmic region does not exist. Flow conditions such as those with strong pressure gradients, low Reynolds numbers and separation fall into this category. Additionally, the accuracy of the method is dependent on the selection of κ and B. For flow over a flat plate, existing data support the general acceptability of the values cited. Under some circumstances, however, the values of κ and B are variable. For example, *Wygnanski* et al. [12.49] found that B exhibits some dependence on the Reynolds number while κ changes little. Additionally, *Nagib* et al. [12.44] provide compelling evidence that κ varies with pressure gradient. For these reasons, it is imperative that κ and B be chosen judiciously in applications where a Clauser plot methodology is implemented. As with all other mean-profile-based methods, another common source of uncertainty can be associated with the method of measuring the velocity profile itself. For example, significant error can be present in Pitot-tube measurements due to their sensitivity to large-amplitude velocity fluctuations, misalignment and low-Reynolds-number effects at the tube opening.

Because the original Clauser plot method was developed for smooth walls, special treatment is necessary for

its use in rough wall flows. Specifically, roughness poses a challenge since it generates an "error in the origin" of the mean profile owing to the well-known downward shift of the inner normalized mean profile, e.g., [12.1,2]. In order to compensate for these challenges, *Perry* and *Li* [12.50] developed a relatively simple iterative method based on Coles formula [12.51]

$$\frac{U}{U_\infty} = 1 + \frac{1}{\kappa}\frac{u_\tau}{U_\infty}\ln\frac{z}{\delta^*} + \frac{1}{\kappa}\frac{u_\tau}{U_\infty}\ln\frac{u_\tau}{U_\infty}$$
$$+ 0.493\frac{u_\tau}{U_\infty}\,, \tag{12.26}$$

where δ^* is the displacement thickness and z is the distance from the crest of the roughness elements. The procedure is then implemented as follows.

1. Using equation (12.26), generate the family of curves relating U/U_∞ to z/δ^* using different values of u_τ/U_∞, and overlay the experimental measurements on this graph.
2. From the graph, select the value of u_τ/U_∞ that corresponds to the parameterized line best approximating the data near $z/\delta^* = 1$.
3. Determine an initial estimate for e, the error in origin, from the portion of the data where $z/\delta^* \ll 1$.
4. Add this estimate for e to the distance from the crest of the element and regenerate the graph.
5. Repeat the entire procedure until a converged value of u_τ/U_∞ is returned.

Relative to the use of this procedure, it is significant to note that (12.26) is based on a wake factor of 0.55. An alternate equation could, however, be easily derived for other values. Additionally, the method of Perry and Li was developed to have the desirable trait of being fairly insensitive to the wake factor.

Viscous Sublayer Profile Method. This method can be considered direct in that it is based upon quantifying the mean gradient of the axial velocity at the wall – or more accurately, very near the wall. According to its definition, the mean shear stress produced at a point on a bounding solid surface by a flowing fluid is given by

$$\overline{\tau}_w = \mu\frac{\partial U}{\partial y}\,, \tag{12.27}$$

where y is the direction that is locally normal to the surface. Thus, for a fluid with known dynamic viscosity μ the requisite task is to experimentally determine the slope of the axial velocity profile at the wall.

Attaining an accurate measure of $\overline{\tau}_w$ from this method first requires the reasonable existence of a linear region in the velocity profile, i.e., a region where

$U^+ = y^+$ in the immediate vicinity of the wall. Certainly, for canonical smooth wall-flows, this approximation is known to hold to a very good approximation [12.2, 52]. In proximity of a point of separation, for example, such a region can rationally be expected to become diminishingly small or even non-existent. Similarly, linear sublayers do not exist (in any quantifiable way) for flows that are not hydraulically smooth. For a reasonably wide range of flows over smooth walls, however, one can expect to find a region within which the mean profile exhibits the linear dependence on distance from the wall as depicted in Fig. 12.1.

Under the vast majority of flow conditions, the physical dimension of the region of linear dependence is small; typically a fraction of a millimeter. Because of this, the sensing dimension of the measurement probe must be very small as well. Although optical sensors such as laser Doppler velocimetry (LDV) and molecular tagging velocimetry (MTV) can be used to measure the sublayer profile, single element hot-wire probes are the predominant sensor of choice owing to their inherently small dimension in the plane parallel to the wall. (Recall that the diameter of a hot wire is typically 5 μm or less.) Given this, the present discussion will focus on the measurement of the sublayer mean profile using a hot-wire probe. Some of the considerations unique to the LDV and MTV techniques are discussed at the end of the next subsection.

Major challenges associated with determining $\overline{\tau}_w$ using (12.27) are (i) determining the region where the mean profile is linear, (ii) accurately and appropriately positioning the sensor in this region, and (iii) accurately calibrating the sensor for the measurements. The region of linear dependence extends from the wall to a small distance above the wall. This region is typically taken to be approximately $y^+ < 5$, although some results suggest it is even smaller [12.53]. In the vicinity of a solid surface, however, thermal anemometry is subject to conduction heat transfer and aerodynamic blockage effects (Sect. 5.2). Thus, for some portion of this region near the wall the hot-wire will produce measurements that overestimate the true velocity value. *Hutchins* and *Choi* [12.54] provide an excellent discussion of this effect relative to accurately determining the mean wall shear stress. They cite the region influenced by wall effects to be approximately $y^+ < 3.5$. For some experimental situations, however, it may be possible to confine this region even closer to the surface by reducing the heating ratio of the sensor, or by using a highly nonconductive surface material. Regarding the latter, *Chew* et al. [12.55] provide a useful study of these wall effects.

In any case, the measurements of interest must then be taken in a region above where wall effects are significant and below the upper bound of the viscous sublayer. For the numbers cited above (by Hutchins and Choi) this region is given by $3.5 < y^+ < 5.0$.

A number of methods are available for positioning the hot-wire probe at a prescribed distance away from the surface. These include the use of mechanical stops and optical displacement sensors. The present authors have also found that locating the probe through the use of a cathetometer (a traversing short-range telescope) can also be effective. In this method, the position of the surface in the immediate vicinity of the probe is located by sighting (with the cross hair of the cathetometer) the point of surface contact made with the tip of a razor blade. The Vernier scale on the traversing scope then allows the sensor position to then be determined and specified by subsequently sighting the probe tip. A repeated set of such measurements, say nine or so, provides a statistically based estimate for the probe position from the wall, as well as an estimate for the uncertainty in this measurement. As noted and discussed by Hutchins and Choi, misalignment of the wire from an orientation parallel to the plane of the surface can also lead to wall-normal positioning uncertainties. The close-up view of the probe through the cathetometer is also useful in minimizing this type of misalignment. Lastly, the probe body should be tilted slightly toward the surface such that the active wire element (tips of the prongs) are positioned to make first contact as the sensor is traversed toward the surface. This serves to minimize aerodynamic blockage effects, and avoids the situation in which the probe body runs into the surface and thus interferes with positioning the sensing wire very close to the surface.

Depending on the details of the experiment, the flow velocity within the viscous sublayer may be too small to accurately calibrate the hot wire using a Pitot tube and pressure transducer. Under such cases, special calibration devices are needed. In this regard, a particularly attractive methodology is to create a laminar flow for which the analytical solution is known. Examples of such devices include the Couette-flow-based calibrator of *Chew* et al. [12.56] and the Poiseuille device of *Yue* and *Malmstrom* [12.57].

12.2.2 Time−Resolved Methods

Relative to the number of techniques designed to measure the time-averaged wall shear stress, those capable of producing time-resolved measurements of the instantaneous wall shear stress are considerably fewer

in number. Two primary reasons for this are that the correlations constituting the basis of indirect techniques are generally not instantaneously valid, and accurately quantifying instantaneous shear stress values requires sensing systems that have both a high-frequency response and are sufficiently small in size. The time-resolved methods discussed in this section are associated with either the direct measurement of the shear force acting over a small element of the surface, or are effectively instantaneous versions of the viscous sublayer profile method discussed above.

Floating–Element Sensors

Perhaps the simplest device (in theory) for measuring wall shear stress is the floating-element sensor. Floating-element sensors directly measure the shear force imparted on a movable, *floating* element portion of the wall. When subjected to flow conditions, the sensor functions either by measuring the amount of force required to keep the element in place or by correlating the displacement of the element with the applied shear force. A major positive attribute of floating-element sensors relative to sensors that indirectly measure shear stress is that no assumptions about the flow field, fluid properties or surface need to be made. Thus, unlike sensors which indirectly measure shear stress, floating-element sensors are not dependent upon the veracity of the correlating function, and therefore are not affected by the errors associated with using the simplifying assumptions needed to develop the correlation.

While floating-element sensors are simple in theory, they are, in practice, often difficult to use. *Winter* [12.59] lists several common challenges associated with the use of floating-element sensors, including:

1. The compromise between the need for an element that is sufficiently large such that the force acting on it has a magnitude that can be measured accurately, and the need for an element small enough to measure local conditions
2. The effect of gaps around the edges of the element
3. Effects due to misalignment of the element
4. Errors associated with pressure-gradient forces.

Other conditions that may influence the performance of the sensor are heat transfer, temperature changes, gravity and/or acceleration, boundary layer suction or injection, leaks, and fluctations of normal forces (which may damage the sensor) during start-up and shutdown [12.59]. Additionally, *Harotinidis* [12.29] notes that larger sensors generally have a reduced temporal resolution, as well as, of course, reduced spatial resolution.
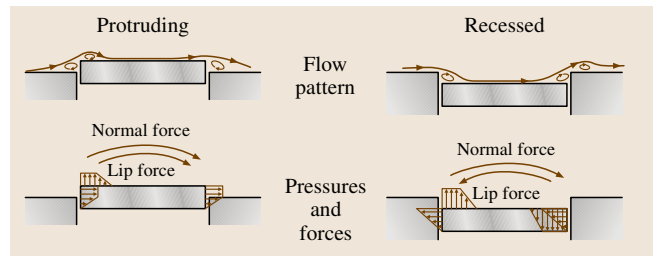

Fig. 12.8 Schematic representation of detrimental floating element misalignment errors (after [12.58])
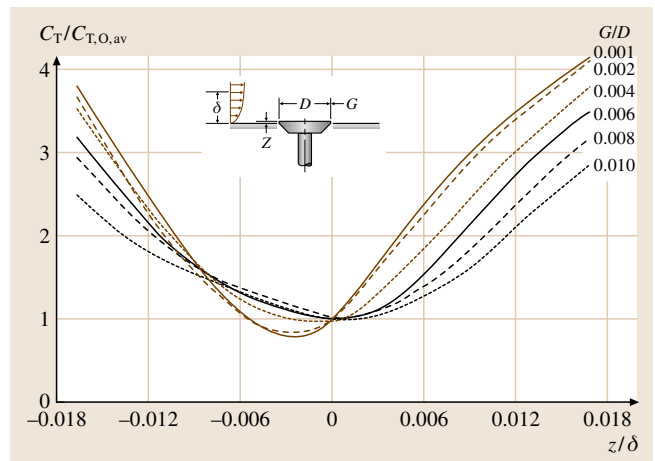

Fig. 12.9 Effects of nondimensional gap and step size on floating element drag measurements (after [12.58])

The studies by *Allen* [12.58, 60] investigated the magnitude of errors associated with gaps, misalignments and element thickness. Errors result from gaps and misalignments since these will cause additional forces under flow conditions that were not present during calibration. A summary of the types of misalignments considered by Allen is shown schematically in Fig. 12.8, while Allen's experimental findings relative to these misalignments are shown in Fig. 12.9. These findings indicate that the ratio of the gap width to the element diameter has a critical effect on the accuracy of the method. Specifically, relatively larger errors result from small gap sizes for the same vertical misalignment, and the thickness of the exposed edge of the floating element has a major impact upon the accuracy of the method. Additionally, *Acharya* [12.61] has shown that uneven pressure distributions will amplify alignment errors by disproportionately acting upon exposed edges of misaligned elements.

In an effort to circumvent the difficulties associated with the presence of gaps, *Frei* and *Thomann* [12.62]

proposed filling the gap around the element with a liquid. Another solution to the gap problem, initially proposed by *Schmidt* et al. [12.63], reduces the gap size using microfabrication techniques; the review of *Lofdahl* and *Gad-el-Hak* [12.64] discusses several micro-electromechanical systems (MEMS)-based floating-element sensors that have since been produced. While the use of MEMS-based floating-element sensors is not yet widespread, *Naughton* and *Sheplak* [12.21] indicate that the errors due to pressure gradients scale favorably for MEMS sensors and that sensor misalignment problems are reduced for microsensors since the sensors are fabricated monolithically.

At its essence, the floating element sensor is a force transducer. The principle of operation for such transducers can invoke (i) single or multiple load cells [12.59], (ii) strain gauges [12.42], or (iii) displacement sensors [12.65]. In all cases, however, the output from the floating element sensor requires calibration relative to known forces. Static calibration involves the application of a series of known constant forces. Often this is most easily accomplished through the use of hanging weights. In this case, care should be taken to utilize very low friction pulleys (e.g., made of teflon) and cables made of materials that do not stretch. Depending on how easily the sensor can be removed from the test section, gravity-based calibration techniques that involve tilting the sensor have also been utilized [12.65]. For time-resolved measurements, the frequency response of the sensor must also be quantified. Under many, if not most, circumstances the floating element sensor can be treated as a one- or two-dimensional second-order spring–mass–damper system. Thus, the frequency response is estimated by applying a known impulsive force and quantifying the time it takes the sensor to return to equilibrium. In turbulent wall-bounded flows the spatial dimension of the floating element is, of course, also an important consideration. Although a comprehensive study of the effects of spatial resolution on miniaturized floating-element sensor measurements has yet to be conducted, it is rational to expect that the criteria discussed above relative to near-wall turbulence measurements are relevant. Generally, fully resolved measurements will require the characteristic dimension of the sensor to be less than about 10 viscous units. Clearly, in most flow situations MEMs sensors are required to satisfy this criterion.

Although the floating-element technique is often difficult to employ, and its accuracy is often challenging to quantify, researchers continue to make use of this method since a priori knowledge of the nature of the flow field is not necessary. Additional improvements in the accuracy and frequency response of the method are expected to follow with further development of MEMS sensors.

Instantaneous Wall Gradient Methods

Under the condition of a smooth wall, single- or multiple-point thermal anemometry based methods can be used to quantify the velocity gradient at the surface. Perhaps the most straightforward version of this involves positioning a single hot wire or a closely spaced vertical rake of wires in the viscous sublayer and acquiring time-resolved measurements of the axial velocity in the region where the velocity profile is linear. In the case where the probe is traversed toward the surface from above, the requirements for obtaining accurate measurements are essentially the same as those discussed previously for obtaining accurate mean shear stress measurements. In one variant, the prongs supporting the hot wire are embedded in a plug that can then be flush-mounted in the surface. This is sometimes termed the hot wire on the wall method [12.66]. In this case, while the operation of the hot wire is standard, its calibration must be modified. Specifically, owing to the very close proximity of the wire to the surface of the plug, it cannot be calibrated for velocity, but rather to the shear stress directly, as are flush-mounted hot-film shear stress sensors.

According to a heat transfer analysis, the static calibration equation for a shear stress sensor is given by [12.67]

$$\overline{\tau}_w{}^{1/3} = AE^2 + B , \qquad (12.28)$$

where E is the bridge voltage, and A and B are calibration constants. The preferred method for calibration of the sensor is in situ, since this avoids errors associated with having to reinstall and align the probe. On the other hand, this also means that another method for measuring the mean wall shear stress must be available for calibration. Popular strategies in this regard are to use either Preston tubes or the Clauser plot technique [12.68]. Owing to the fact that these techniques are correlation-based, the resulting calibrated sensor can not be viewed as an independent means for measuring $\overline{\tau}_w$. Given that the primary goal of such a sensor is to measure the τ_w fluctuations, this does not necessarily pose a major problem. Of course, if the measurement facility is a fully developed pipe or channel flow, then one may calibrate against the mean pressure drop, and thus generate an analytically well-founded calibration.

As expected, an important concern for flush-mounted shear stress sensors is their spatial resolution,

and the aforementioned desirability of the sensor dimension to be less than about 10 viscous units. Perhaps an even greater concern is the loss of temporal resolution at high frequencies resultant from the thermal effects associated with the sensor substrate. Specifically, the critical issue is the heat transfer to the fluid relative to the heat transfer to the substrate [12.69]. While corrections for these effects have been developed, the empirical evidence indicates that they generally do not fully account for the attenuating effect. Thus, it is best to use fluid/substrate contributions that result in most of the heat transfer to the fluid [12.66]. For this reason, measurements in water exhibit superior performance to those in air. As with standard hot-wire anemometry, multiple wire configurations can be used to measure more than one component of velocity. In this regard, a v-array plug provides measurements of the fluctuating axial and spanwise wall velocity gradients, $\partial u/\partial y$ and $\partial w/\partial y$, respectively.

As a final note regarding flush-mounted sensors, it is also worth mentioning that in liquid flows one may also use electrochemical mass transfer probes to infer the wall shear stress fluctuations. This method relies on the correlation between the concentration gradient and velocity gradient at the surface. The development and implementation of these sensors is largely due to the extensive body of work conducted by *Hanratty* and his coworkers [12.42].

Of course, measurements of the instantaneous wall gradient are possible as long as spatially and temporally well-resolved axial velocity measurements can be accurately acquired in the viscous sublayer. In this regard, at least two optical techniques have been successfully employed.

Continuing refinement of LDV techniques have produced several systems capable of making sublayer velocity measurements in flows beyond low Reynolds number. Of course, a common characteristic of suitable systems is an especially small measurement volume. For example, in the study by *DeGraff* and *Eaton* [12.13], the dimensions (major and minor axes) of the ellipsoidal measurement volume were 65 µm × 35 µm. This was achieved by special focusing optics and using side scatter collection optics [12.70]. LDV measurements acquired close to a surface are also susceptible to negative influences associated with optical access and surface interference, as well as velocity bias associated with high shear across the measurement volume [12.18]. Regarding the latter, *Durst* et al. [12.71] have devised correction methods for the various moments of the velocity fluctuation probability density function. Owing

to the low-speed flow in the sublayer, adequate seeding also requires careful attention.

Because it provides very closely spaced data instantaneously along a line, single- or multiple-line molecular tagging velocimetry (MTV), is especially well suited for wall gradient measurements. As discussed in Sect. 5.4, the basic idea underlying MTV is that fluid velocity data can be derived by tracking a pattern of excited, long lifetime, phosphors that have been mixed within the fluid and subsequently excited by laser light. Typical hardware, data acquisition and data reduction methods employed in the line version of the technique in wall-bounded flows are described in the studies by *Hill* and *Klewicki* [12.72–74] and the references therein. More-general applications of MTV and its extensions to two-component measurements are given by *Koocheshfahani* and coworkers [12.75–77]. In the MTV line technique, a series of laser lines are used to excite the dissolved phosphor, and a gated camera is used to acquire the initial and time-delayed images of these lines. If the fluid is moving, these lines of excited phosphor are displaced according to the local flow velocities. The essence of the MTV technique is that velocity field data are found by tracking this displacement over a sufficiently short time duration such that a Lagrangian approximation (e.g., $u = \Delta x/\Delta t$) becomes valid.

With the line displacement and time delay between images known, the velocity may be estimated. Uncertainties are associated with the quantification of Δx, and to a lesser degree Δt. Furthermore, root-mean-square (RMS) and mean bias errors (relative to the true line location) can be associated with the line position locating algorithms. Automated image-processing-based methods do, however, allow the line displacement to be determined to within a small fraction of a pixel. The line technique is also susceptible to an error associated with the effect of having a velocity component parallel to the line. These errors result from the inability to identify and subsequently track unique fluid elements on the line. As a percentage of the instantaneous streamwise velocity this error can be expressed as

$$\frac{\Delta u}{u} = \Delta t \frac{v}{u}\frac{\partial u}{\partial y} , \tag{12.29}$$

where u, v and $\partial u/\partial y$ are instantaneous quantities. For the near-wall region of the boundary layer, *Klewicki* and *Hill* [12.73] showed that this effect causes about a 1% bias error.

For typical lens magnifications, one can obtain well over 20 measurements per millimeter along the

MTV line. This density of data is, of course, attractive when seeking to curve-fit to obtain the local slope at the surface. Owing to light reflections, however, it is often difficult to acquire data exactly at the sur-face. Measurements to within about $y^+ = 1$ have been reported [12.73]. The temporal resolution of the technique is limited by the camera frame rate and the laser repetition rate.

12.3 Boundary-Layer Stability and Transition

Stability and transition experimentation is no trivial task and should be undertaken by only the most serious researcher. The basic idea of an instability is that small disturbances in the flow can have large effects on the basic state, leading in some instances to additional instabilities. Small changes in an experimental set-up and measurement can introduce unanticipated disturbances that can complicate the flow or skew the interpretation of the results. When transition to turbulence proceeds through loss of stability, the process critically depends on these small effects. Thus, unlike many situations in turbulent boundary layers, measurements of stability characteristics require a special sensitivity to environmental conditions. The subsequent sections aim to highlight some of the particular details required to successfully complete a stability experiment and to advise against common mistakes throughout the process.

12.3.1 The Process of Transition for Boundary Layers in External Flows

In fluids, turbulent motion is usually observed rather than laminar motion because the Reynolds-number range of laminar motion is generally limited. The *transition* from laminar to turbulent flow occurs because of an incipient instability of the basic flow field. This instability intimately depends on subtle, and sometimes obscure, details of the flow. The process of transition for *boundary layers in external flows* can be qualitatively described using the following (albeit oversimplified) scenario.

Disturbances in the free stream, such as sound or vorticity, enter the boundary layer as steady and/or unsteady fluctuations of the basic state. This part of the process is called *receptivity* [12.78] and although it is still not completely understood, it provides the vital initial conditions of amplitude, frequency, and phase for the breakdown of laminar flow. Initially these disturbances may be too small to measure and they are observed only after the onset of an instability. A variety of different instabilities can occur independently or together and the appearance of any particular type of instability depends on Reynolds number, wall curvature, sweep,

roughness, and initial conditions. The initial growth of these disturbances is described by *linear* stability theory (i. e., linearized, unsteady Navier–Stokes). This growth is weak, occurs over a viscous length scale, and can be modulated by pressure gradients, surface mass transfer, temperature gradients, etc. As the amplitude grows, three-dimensional and nonlinear interactions occur in the form of *secondary* instabilities. Disturbance growth is very rapid in this case (now over a convective length scale) and breakdown to turbulence occurs.

Since the linear stability behavior can be calculated, transition prediction schemes are usually based on linear theory. In the case of streamwise instabilities and low-disturbance environments, linear theory does very well in predicting the stability behavior. However, since the initial conditions (receptivity) are not generally known, only correlations of transition location are possible and, most importantly, these correlations must be between two systems with similar environmental conditions [12.79].

Thus, linear theory is the foundation of streamwise instabilities in low-disturbance flows. A brief review of the nomenclature of linear theory precedes the description of experimental methods. It is assumed that the reader understands the fundamental ideas of hydrodynamic stability found in [12.79–81]. Background material on transition can be found in [12.82] and [12.83].

12.3.2 Nomenclature of Linear Theory

As a reference point, start with an incompressible, isothermal flow over a flat plate with zero pressure gradient. The basic state is assumed to be locally approximated by the parallel flow $\boldsymbol{V} = [U(y), 0, 0]$, where $(\hat{x}, \hat{y}, \hat{z})$ are the dimensional streamwise, wall-normal, and spanwise directions, respectively. Dependent and independent variables appearing as $\hat{q}$ are dimensional, otherwise they are dimensionless. Lengths and velocities are made dimensionless with the scales L and U_∞, respectively. Two-dimensional disturbances are superposed on the Navier–Stokes equations which are then

linearized. Assuming a normal-mode disturbance of the form

$$q'(x, y, t) = q(y) \exp[i(\alpha x - \omega t)] + \text{c.c.}, \quad (12.30)$$

where q' represents a real disturbance quantity such as pressure or a velocity component. For spatially varying disturbances, the use of (12.30) results in the Orr–Sommerfeld equation (OSE) given by:

$$(D^2 - \alpha^2)^2 \phi - iR[(\alpha U - \omega)$$
$$\times (D^2 - \alpha^2)\phi - (\alpha D^2 U)\phi] = 0, \quad (12.31)$$

where c.c. means complex conjugate, $D = d/dy$, ϕ is complex and represents the disturbance stream function, $\phi(0) = D\phi(0) = 0$, $\phi(y \to \infty) \to 0$, ω is real, $\alpha = \alpha_r + i\alpha_i$, $-\alpha_i$ is the spatial growth rate, $c = \omega/\alpha_r$ is the phase speed. Here the dimensional frequency is conserved and the length scale is $L = \sqrt{\nu \hat{x}/U_\infty}$. These give rise to the following definitions

$$R = \frac{U_\infty L}{\nu} = \sqrt{\frac{U_\infty \hat{x}}{\nu}}, \quad (12.32a)$$

$$F = \frac{\omega}{R} = \frac{2\pi f \nu}{U_\infty^2} = \text{constant}. \quad (12.32b)$$

The eigenvalue problem reduces then to finding $\alpha = \alpha(R, F)$. The locus of points for which $\alpha_i(R, F) = 0$ is called the neutral stability curve. For a given F in Blasius flow, R is double-valued. The smallest value, R_I, occurs at branch I and the largest value, R_{II}, occurs at branch II. Between these two Reynolds numbers, the flow is unstable. Transition depends on the measure of growth between R_I and R_{II}. The Reynolds number below which the flow is stable for all F is called the minimum critical Reynolds number Re_{crit}.

Some also have used the displacement thickness δ^* or the momentum thickness θ as the normalizing length with an attendant redefinition of the Reynolds number. All of these choices are appropriate for boundary-layer scaling. However, since no universal Reynolds number criterion appears with either R_{δ^*} or R_θ for other boundary-layer flows, the use of these scales just adds a superfluous constant. On the other hand, the use of $L = \sqrt{\nu \hat{x}/U_\infty}$ makes the dimensionless wall-normal coordinate $y = \eta$ (the Blasius similarity variable) and makes the boundary-layer Reynolds number the root of the x-Reynolds number.

In a Blasius boundary layer, R measures distance along the plate and a disturbance at the reduced frequency F is called a *Tollmien–Schlichting* (T–S) wave. Under certain conditions this wave is amplified, can interact with three-dimensional (3-D) disturbances,

secondary instabilities can occur, and breakdown to turbulence can result. The generation and growth of these waves as they relate to disturbances in the basic state will be of particular interest during the experiment.

12.3.3 Basic Rules for Boundary–Layer Stability Experiments

Regardless of whether the experimental objectives are transition control, three dimensionality, secondary instabilities, nonlinear breakdown, or receptivity, the superseding rules of conducting a stability experiment are: (1) the linear problem must be correct, and (2) initial conditions must be provided for theory and computations. These rules can be considered prime directives.

Rule One
The first rule is to get the linear problem correct. Correlation of the experimental data with linear theory (in the appropriate range) ensures that the basic state is probably correct. Usually unintended weak pressure fields change the stability behavior but are not detected in the basic state measurements (Sect. 12.3.4).

Rule Two
Full documentation of physical properties, background disturbances, initial amplitudes, and spatial variations must be provided to the analyst. It is very important to measure, whenever possible, the free-stream environment (a subsection of Sect. 12.3.4 covers the details of measurements of the free-stream turbulence and sound). Any worthwhile stability experiment is going to be accompanied by a computational effort. The experimentalist needs to be able to give as many initial conditions to the analyst running the computational simulations so that an accurate comparison can be made between both methods. This includes, of course, the specification of coordinates since experiments are done in test-section coordinates while computations are done in body-oriented coordinates. The experimentalist should also heed flow symmetry requirements that the computationalist readily assumes but requires some work to achieve in the wind tunnel (see Sect. 12.3.4).

Although these seem like simple requirements, the literature has many examples of experiments that ignore these precepts. In the sections that follow, examples are discussed that illustrate the difficulty of establishing these two rules. However, all of the examples are real, correctable effects. The more advanced practitioner is referred to the *transition study group guidelines* for transition experiments [12.84].

12.3.4 Experimental Techniques

Use a Flat Plate that is Flat

For a Blasius boundary-layer experiment, a flat plate is needed; however, not all methods of manufacturing a flat plate are equally desirable. Plates originating from rolled metal are generally not recommended since the wavy-surface contour can produce a streamwise periodic pressure distribution, as was found on the original Schubauer and Skramstad plate [12.85] (now at Texas A&M). The Klebanoff flat plate [12.86] used at NBS was treated with a 1.8 m-diameter grinding disk. This option can produce satisfactory results, but is often expensive. The Saric flat plate [12.87] used at Virginia Tech and Arizona State, had a 20 mm paper honeycomb sandwiched between two 1 mm aluminum sheets in the manner that inexpensive billiard tables are fabricated. A rule-of-thumb waviness criterion for any plate intended for stability experiments is $\varepsilon/\lambda_{\mathrm{T-S}} < 10^{-3}$, where ε is the waviness height and $\lambda_{\mathrm{T-S}}$ is the T–S wavelength. Both the Klebanoff plate and the Saric plate had a ratio of $\varepsilon/\lambda_{\mathrm{T-S}} < 10^{-4}$.

Provide a Means for a Leading Edge

The shape of the leading edge has a large effect on the resulting flow field. *Schubauer* and *Skramstad* [12.85] used a sharp leading edge, which was drooped at a negative angle of attack to avoid separation that can occur with a sharp tip. *Klebanoff* [12.86] also chose this type of leading edge, but instead addressed the problem of separation at the tip by including a trailing-edge flap to introduce circulation and thus place the stagnation line on the test side of the plate. The difficulty with either technique is that it is difficult to simulate computationally. Another possible option is an elliptical leading edge with a trailing-edge flap, as shown in Fig. 12.10.

An ellipse with a major/minor axes ratio greater than 6:1 avoids a separation bubble on the leading edge. An ellipse has zero slope at the flat-plate intersection but has a discontinuity in curvature at that point which could be a receptivity location. The curvature discontinuity can bias an acoustic receptivity experiment so *Lin* et al. [12.88] proposed using a *modified super ellipse* whose contour follows

$$\left(\frac{\hat{y}}{b}\right)^2 + \left(\frac{a-\hat{x}}{a}\right)^m = 1 \, , \quad m = 2 + \left(\frac{\hat{x}}{a}\right)^2 . \quad (12.33)$$

Here, the origin is at the stagnation line and a and b are the major and minor axes of the ellipse. With this profile, the curvature goes continuously to zero as $\hat{x} \to a$. The aforementioned Klebanoff plate (now at
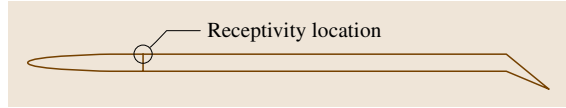

Fig. 12.10 Flat plate with a trailing-edge flap

Texas A&M), was modified by the author for receptivity experiments [12.89, 90] by machining directly on the plate, a 20:1 super ellipse on one end of the plate and a 40:1 super ellipse on the other end. Machining the leading edge directly on the plate avoids junction discontinuity issues that could also be a receptivity site.

Global Pressure Gradient

Whether one uses a blunted flat plate or a sharp flat plate at negative angle of attack, a leading-edge pressure gradient will be present and a finite distance is required for pressure recovery. Once a zero pressure gradient is obtained, the boundary-layer flow is Blasius, but referenced to a different chordwise location, $\hat{x} = \hat{x}_{\mathrm{v}}$. Thus, there is a *virtual* leading edge from which the measurements and the Reynolds number must be referenced. If this is unaccounted for, it is very easy to have 20–30% errors in $\hat{x}$ (and 10–15% errors in R). For example, in order for theory to agree with the linear part of the well-known nonlinear work of *Klebanoff* et al. [12.86], one must apply a correction to $\hat{x}$ [12.91].

To be ensured of the correct streamwise location, measure the displacement thickness δ^* and then calculate the virtual location and Reynolds number with respect to the Blasius boundary-layer profile

$$\delta^*(\text{measured}) = \int_0^\infty (1 - \hat{u}/U_\infty) \, \mathrm{d}\hat{y} \, , \quad (12.34)$$

where $\delta^*(\text{Blasius}) = 1.72\sqrt{\nu\hat{x}/U_\infty} \neq \delta^*(\text{measured})$. The virtual location is given by

$$\hat{x}_{\mathrm{v}} = \left(\frac{\delta^*(\text{measured})}{1.72}\right)^2 \frac{U_\infty}{\nu} \, , \quad (12.35)$$

$$R = \left(\frac{U_\infty \hat{x}_{\mathrm{v}}}{\nu}\right)^{1/2} . \quad (12.36)$$

The effects of not differentiating between the virtual and geometric locations are repeatedly demonstrated in early stability literature. Present-day researchers must be wary of which location, virtual or geometric was used to obtain transition Reynolds numbers in past literature.

Because of traverse effects and tunnel side-wall blockage, $\hat{x}_v$ may actually change with different chordwise measurements. Therefore, δ^* should be measured (and R calculated) at each location. With modern, computer-controlled experiments this is not a problem. On the other hand, it has been shown by *Klingmann* et al. [12.92] that it is possible to design the leading-edge pressure gradient on the flat plate to eliminate the virtual leading edge. Figure 12.11 shows a series of velocity profiles by the author that demonstrates a constant $\hat{x}_v$ when traverse effects are eliminated.

Local Pressure Gradient

It is difficult to measure small changes in the pressure coefficient C_p accurately. Thus, the flow may not be locally Blasius and the stability characteristics may be quite different. For example, a decrease in C_p of approximately 1% over 100 mm corresponds to a Falkner–Skan pressure gradient parameter, β, of approximately 0.1. For $\beta = +0.1$, the minimum critical Reynolds number, Re_{crit}, [based on Sect. 12.3.7] is increased by a factor of 3. In other words, the streamwise location is increased by a factor of 9.

The neutral stability curve, shown in Fig. 12.12 compares OSE, the nonparallel theory (PSE), and DNS with experiments. What is important is that OSE (dashed line), PSE (solid line), and DNS (points on the solid line) agree very well. The experiments only agree at low frequencies and high Reynolds numbers. The measured
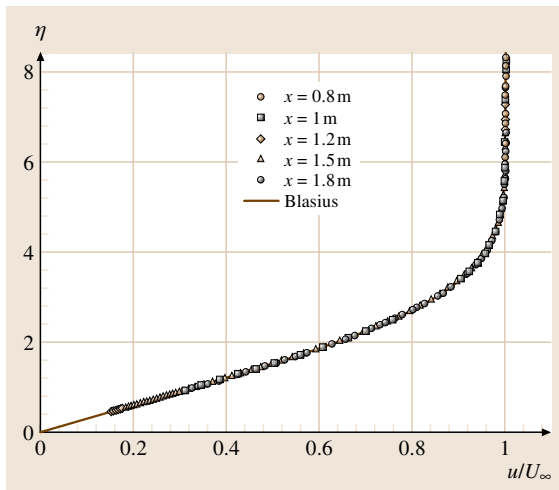

Fig. 12.11 Five measured velocity profiles at $x = 0.8, 1.0, 1.2, 1.5,$ and 1.8 m superposed on the Blasius flow calculation. Streamwise location corrected for the virtual leading edge. The free-stream speed is 12 m/s
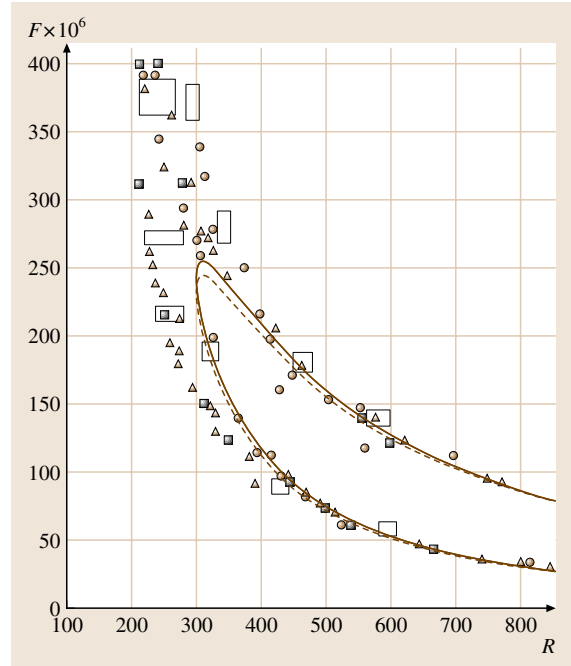

Fig. 12.12 Blasius neutral stability curve. Comparison between experiment, DNS, PSE, and OSE [12.93]

Re_{crit} is around 230 and the calculations all give a value of 300. *Saric* [12.94] conjectured that this difference is due to the extreme sensitivity to the smallest of pressure gradients (in this case adverse) that exist near branch I. This has been confirmed by *Klingmann* et al. [12.92] who designed an experiment to avoid a pressure gradient at branch I and whose data fall on the theoretical neutral stability curve. Thus, the historical discrepancy between theory and experiment has been resolved. There are other problems with the experiments and these are discussed below.

A weak adverse pressure gradient can also explain why instabilities are measured at dimensionless frequencies, $F > 250 \times 10^{-6}$, contrary to theory. The range of unstable frequencies could increase dramatically if the measurements were made in the weak adverse pressure gradient region of the recovery zone of the leading edge. Because of the low Reynolds number needed, the measurements of Re_{crit} [12.95] were conducted too close to the leading edge and too close to the disturbance source.

With extreme care one may be able to measure $\Delta C_p \approx 0.3\%$. This may not be enough. However, one could measure $U(y)$ and calculate the shape factor, $H = \delta^*/\theta$. Here, $\beta = +0.1$ corresponds to $\Delta H = 7\%$
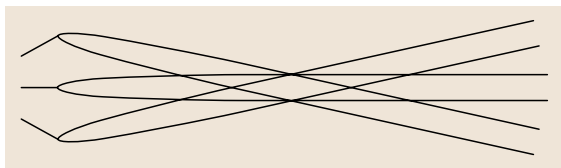
Fig. 12.13 Plate vibrations change the stagnation line

compared to $\Delta C_p = 1\%$. Thus, measurement of changes in the shape factor is more reliable than ΔC_p. One should already have $U(y)$ at each streamwise location and hence the pressure gradient can be verified at no additional work.

For Blasius flow, it is recommended that the plate be adjusted so that $H = 2.59 \pm 0.005$. Moreover, placing a boundary layer trip on the backside of the model helps avoid differential blockage problems by fixing the transition location on the non-test side. Velcro is the recommended trip since a 6 mm-high strip can excite all of the important scales.

This discussion concludes that whereas the zero-pressure-gradient case is an accepted reference test case, it is a rather sensitive and perverse test condition. The author's experience with boundary layers on wings shows that modest pressure gradients ameliorate the sensitivity to small ΔC_p. At the same time, it needs to be recognized that one should avoid measurements of Re_{crit}. Not only is this a very difficult measurement to interpret, but changes in Re_{crit} have very little to do with transition.

Fig. 12.14 Schematic and data of Δp measurement to achieve symmetric flow

Probe and/or Plate Vibration

If the probe support is vibrating in a direction transverse to the shear layer, the hot wire will measure different levels of the direct-current (DC) component, which in turn appear as temporal fluctuations in the alternating-current (AC) component. Carbon composites work well to stiffen a particular direction of the probe support if vibration is suspected.

Plate vibration is a very serious source of error that should be avoided at all costs. These vibrations cause oscillations in the stagnation line, as shown in Fig. 12.13, that create the initial conditions for T–S waves.

The author has used a laser vibrometer to map the vibrations of the leading edge. These studies showed vibration amplitudes on the order of one micron. If a laser vibrometer is not available, it is important to use a low-mass accelerometer. In any case, some diagnostic tool is needed to ensure that the oscillations are not in the T–S pass band.

Symmetric Flow

When providing a data base for computations of the leading-edge region, it is realistic to establish symmetric flow as an appropriate reference point. The trailing-edge flap is used to control the position of the stagnation line (the shape factor and pressure measurements will determine the plate angle). The pressure difference between the two sides of the leading edge is monitored while the trailing-edge flap angle is changed. When $\Delta p = 0$, the flow is symmetric. It is important to measure Δp in a region of large dp/dx to maximize the sensitivity of the measurement. If differential blockage is minimized and the non-test side boundary layer is tripped properly, it is possible to have the same flap setting at different speeds. Figure 12.14 shows the relationship between flap angle Δp and free-stream speed (unit Reynolds number).

12.3.5 Wind Tunnel Environment

Model Location in the Test Section

Prior to mounting the plate in the test section, all of the vortical modes must be determined. The contraction cone has the tendency to amplify the corner vortices and produce some large scale vortical motions in the test section that may take the form of those shown in Fig. 12.15. This is especially true of tunnels with contraction ratios greater than 6. This weak secondary motion is difficult to measure directly but can be observed by spanning the tunnel with a heated wire. By doing wake scans with a *cold* hot wire (no overheat) at different streamwise locations, the temperature nonuniformity can be tracked
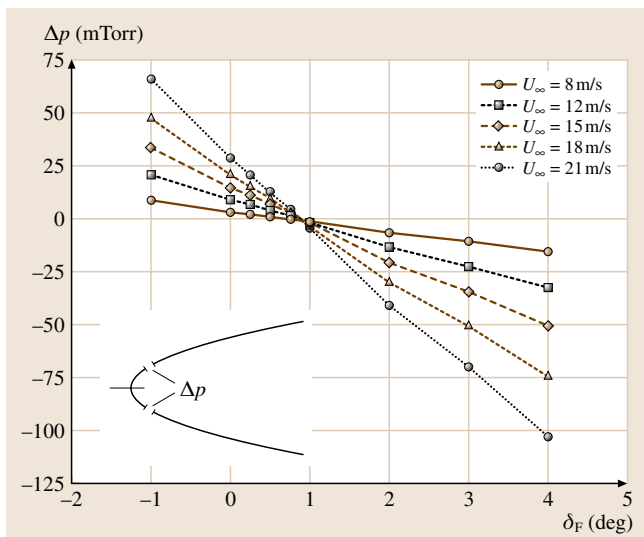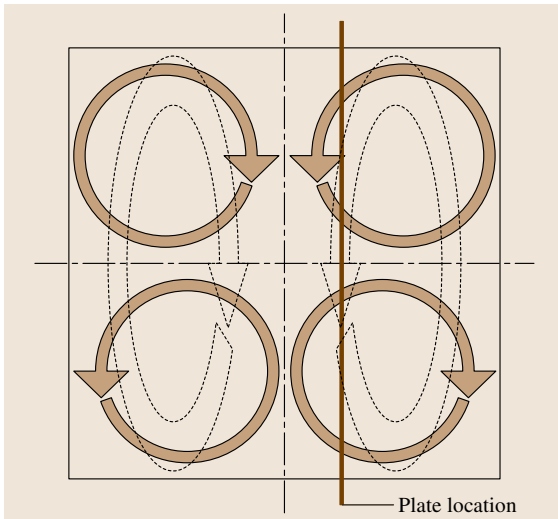
Fig. 12.15 Determination of tunnel nodes and plate placement

and any in-plane rotation can be observed. The rotational nodes can be determined and the plate placed away from these nodes. Acoustic modes will also exist in the test section and these nodes must be avoided as well.

A good rule of thumb is never to mount the plate on an axis of symmetry or at locations $1/N$ of the tunnel span where $N = 2, 3, 4$, etc. Generally, a good location is somewhere between 0.38 and 0.45 unit span.

Free Stream Disturbances: Turbulence and Sound

Ordinary wind tunnels have turbulence levels high enough to mask the appearance and growth of T–S waves. It was not until *Schubauer* and *Skramstad* [12.85], in a tunnel designed for low turbulence, that a successful boundary-layer stability experiment was conducted. It was also recognized at that time that the flight environment also had low turbulence with regard to influencing stability and transition. After the initial success of these experiments, it was recognized that something more than reducing u' fluctuations was needed to advance the knowledge base.

Unknown receptivity issues such as the roles of free-stream turbulence and sound in creating T–S waves and 3-D structures inhibit the understanding and control of transition. It is certainly clear that a naked statement of RMS streamwise fluctuations, $|u'|/U_\infty$, is not enough to describe a particular wind-tunnel environment. Free-stream disturbances are composed of rotational disturbances (turbulence) and irrotational dis-

turbances (sound). Each plays a different role in the transition process. Cross-flow waves are very sensitive to free-stream turbulence level [12.96] while T–S waves are very sensitive to free-stream sound [12.90]. *Naguib* et al. [12.97] demonstrate a good second-order method for separating sound from turbulence that is easy to implement in real-time data acquisition.

Until we really understand the receptivity mechanisms, it is important to document the free-stream disturbance environment as completely as possible. In addition to $|u'|/U_\infty$, one should quote, in order of importance: (1) pass band and spectrum for all measurements, (2) spatial correlation measurements of all components to separate turbulence from sound, (3) flat-plate transition Reynolds number at different unit Reynolds numbers, and (4) $|u'|/U_\infty$, $|v'|/U_\infty$, and $|w'|/U_\infty$ at different positions. A general summary of flow-quality issues is found in [12.98] and a typical tunnel certification is given by [12.99].

It has been argued [12.92] that it is not necessary to have free-stream turbulence levels down to 0.04% U_∞ in order to measure T–S waves. This is a naïve statement that is only true when one knows where one is looking and one knows what one is measuring. For example, *Kendall* [12.100] has been measuring T–S waves in high-disturbance environments for years. There are two relevant points that need to be mentioned justifying a low-disturbance free stream: (1) one can always systematically increase free-stream turbulence [12.100] and study its effects and (2) different (unknown) breakdown mechanisms that are characteristic of the low-disturbance flight environment may be missed in a high-disturbance free stream. The observations of the subharmonic mechanisms [12.101, 102] fall into this category.

Another argument for low-turbulence levels can be made when streamwise vortical structures in the basic state produce a weak spanwise periodicity that is strongly susceptible to secondary instabilities. These spanwise variations were carefully documented by *Klebanoff* et al. [12.86], *Nishioka* et al. [12.103], and *Anders* and *Blackwelder* [12.104]. They strongly influence the type of breakdown to transition that is observed [12.101, 105]. These spanwise variations were not observed in the low-turbulence tunnels in Arizona, Novosibirsk, Sendai, or Stockholm. It turns out that these tunnels had slightly lower turbulence levels and that the combination of higher turbulence levels and micro surface roughness caused transient modes to grow and create the streamwise vorticity within the boundary layer. This is a good example of why it is necessary

to be able to do spanwise measurements in the tunnel and within the boundary layer. Finding a turbulence level at one spanwise location does not guarantee the same turbulence level at other spanwise locations. As a general reminder, tape or junctions act similar to the micro surface roughness in that they are receptivity locations and are to be avoided on the test surface of the plate. Even though one may have a two-dimensional (2-D) roughness with an $Re_k = O(0.1)$, this is still a strong receptivity source [12.90, 106]. Therefore, in order to establish the initial conditions, one should provide the measured three-dimensional amplitude modulation within the boundary layer for comparisons with theory and computation.

12.3.6 T–S Measurements

Controlled T–S Waves – Internal Disturbance Sources

Knapp and *Roache* [12.107] tried to use the background disturbances as the source of the T–S waves and observed intermittent behavior that compromised their hot-wire measurements. It becomes necessary to fix the wave in the streamwise direction and do phase-correlated measurements. The use of an artificial disturbance source will fix the amplitude and phase at one location in order to systematically track stability and transition events. The use of a vibrating ribbon to create 2-D waves has been around since *Schubauer* and *Skramstad* [12.85]
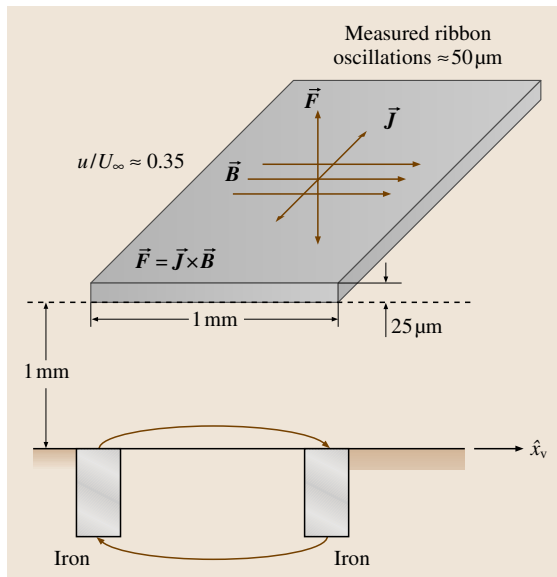
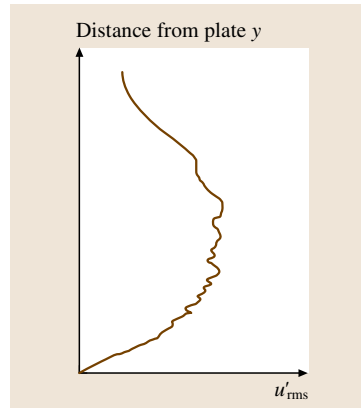**Fig. 12.16** Schematic of a vibrating ribbon

Fig. 12.17 Disturbance profile close to the ribbon

who used the idea of the Lorentz force generated by an alternating current in the ribbon in the presence of a stationary magnetic field. This is shown in Fig. 12.16. *Sreenivasan* et al. [12.108] has used the same principle on a wire in a slot. *Corke* and *Mangano* [12.102] have successfully used segmented heated wires for producing both 2-D and 3-D waves.

When the vibrating ribbon or wire is uniformly loaded, the displacement is of the form of a catenary. Therefore, a sufficiently long ribbon should be used to avoid end effects. The ribbon placement in the wall-normal direction is typically ideal (minimum displacement) if located at or near the critical layer $[U(y) = c = \omega/\alpha]$.

Even though the 2-D wave is phase correlated when using a vibrating ribbon, the interaction of this wave with the background disturbances has a random character. The Λ-vortices observed by *Saric* and *Thomas* [12.101] for different types of breakdown meandered in the span direction. Although not reported, the subharmonic measurements of *Kachanov* and *Levchenko* [12.109] were random and eyeball conditional sampling was used. The only solution is to introduce the 3-D disturbance directly with segmented heating elements [12.102]. The technique consists of using one continuous wire for the 2-D wave and a set of segmented wires, whose individual phase is controlled, for the 3-D wave.

A disturbance source such as an air jet, or heated wire, or vibrating ribbon, locally creates a disturbance that is not just a T–S wave (Fig. 12.17) but has all of the eigenmodes. A T–S wave is just one of the modes in the distribution. A relaxation distance is required to attenuate the more stable modes so that the least stable (the T–S wave) remains. If measurements are made within this relaxation distance some strong stabilizing effects may be measured. One should determine the relaxation distance

downstream of the disturbance source. This would depend on the type of source used, but it should be in the range of about 10 boundary-layer thicknesses. This can be verified by first comparing $\left|u'(y)\right|$ with linear theory. Local growth rates should also be compared as a function of input amplitude. These comparisons should be documented if it is required to measure close to the disturbance source.

One would like to carry out stability measurements over a wide range of Reynolds numbers while keeping the disturbance source fixed. Unfortunately, a typical 2-D disturbance source has a finite span and *Mack* [12.110] showed that the domain of dependence of a finite span disturbance source propagates from each end toward center span at an angle of approximately 12° as shown in Fig. 12.18.

Outside of this triangular domain, the disturbance amplitude is different from linear theory. This is analogous to the boundary-condition domain of dependence in hyperbolic systems. If w is the span of the disturbance source and L is the distance in x from the source, then the centerline measurements should be made such that $L/w < 2.3$. *Ross* et al. [12.95] had a vibrating ribbon span of only 250 mm and took measurements 1 m away. Just as one is limited in the useful chord of the model due to sidewall contamination, the distance downstream of the disturbance is similarly limited. For off-centerline measurements, this value is obviously smaller.

When one attempts to study nonlinear wave interactions, the nonlinearities of the disturbance source impose different initial conditions on the nonlinear components [12.87]. For example, if one wishes to study the nonlinear interaction of waves with two frequencies f_1 and f_2, when the disturbance source, such as a vibrating ribbon, is oscillated at too high an amplitude, the disturbance source inputs $2f_1$, $2f_2$, $f_1 - f_2$, $2f_1 - f_2$, etc. into the boundary layer. As part of another difficulty, when one attempts to invoke active wave cancelation into the boundary layer through a disturbance source, a feedback signal is processed by the computer and relayed to a disturbance source. However,
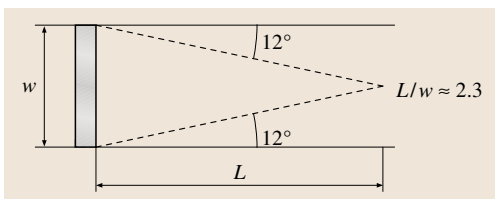
the digital-to-analog (D/A) converter is a low-pass filter, the vibrating ribbon is a low-pass filter having a typical linear oscillator response, and the boundary layer is a band-pass filter/amplifier having its unique response curve. Thus the boundary-layer response is much different from the original input signal. First, one must always directly measure the disturbance-source response and the boundary-layer response in order to establish the initial conditions [12.87]. In the case of a vibrating ribbon, the disturbance source response can be measured with an end-effect inductance probe. A tailored boundary-layer response can be obtained using inverse Fourier techniques [12.111].

Controlled T–S Waves – External Disturbance Sources

If an external sound source is used as a source of disturbance energy, say in a receptivity experiment, then the boundary-layer measurement at a particular frequency will contain probe vibrations and a component of the sound wave in addition to the T–S wave. It is easy for external sound to force, at the oscillation frequency, the mechanical system holding the hot wire. The external sound field generates a Stokes layer imbedded inside the boundary layer. All of these signals are at the same frequency and if these signals are of comparable amplitude to the T–S amplitude, one cannot obtain the usual T–S profile unless some special techniques are used to extract the T–S wave. It is for this reason that older publications with sound/stability interactions are not reliable.

This author has tried: (1) taking advantage of the exponential growth of the T–S wave so that it is larger than the background [12.106]; (2) the idea of using polar plots to separate the long-wavelength Stokes wave from the short-wavelength T–S wave [12.112]; (3) the idea of using a wavenumber spectrum using closely spaced points in the x direction [12.98]; (4) the idea of using differential surface-pressure ports [12.100]. For one reason or another, none of these techniques are satisfactory and are not recommended. The details are given in [12.113]. The major problems lie in complicated duct acoustics and reflected waves from the diffuser.

The only technique found to work is the pulsed-sound technique [12.89, 90]. The technique uses pulsed sound and is simple, effective, and lends itself to understanding the behavior of the T–S wave. From linear theory, the maximum of the T–S wave propagates at approximately one third of the free-stream speed (about 1% of the speed of the downstream-traveling sound wave). Using this fact, the traveling T–S wave can
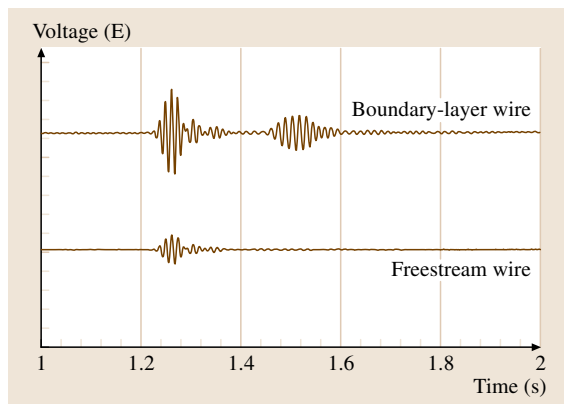

Fig. 12.18 Triangle of acceptable measurement area

Voltage (E)

Fig. 12.19 Time traces of the free-stream wave and the boundary-layer wave

be isolated from the acoustic disturbance and associated Stokes wave by sending bursts of sound into the test section. The initial sound burst is first measured and fractions of a second later, after the sound wave has passed, the slower-traveling T–S wave is measured. Figure 12.19 shows a time trace depicting the sound-burst wave sensed by hot wires in the free stream and boundary layer and the trailing T–S wave measured by the boundary-layer wire for $R = 1140$, $F = 56 \times 10^{-6}$, $f = 80$ Hz and $x = 1.8$ m. The T–S wave profile obtained with this method compares very well with OSE solutions.

There are three ways to implement this technique: (1) use the RMS amplitude of the wave packet [12.89]; (2) use the magnitude of the complex Fourier coefficient for each frequency present in the wave packet [12.90]; (3) analyze the signal in the frequency domain [12.114]. The frequency-domain approach [12.114] appears to be the best means to correctly describe the receptivity and linear amplification process of multiple-frequency signals. This is because as wave packets travel downstream, high-frequency components of the spectra, which are present initially due to the finite extent of the pulse, decay. Meanwhile, the low-frequency components in the amplified T–S pass band grow.

A feature of short sound bursts is that since they are limited in the time domain, they are extended in the frequency domain. Thus, a single sound pulse (a single frequency sine wave within an amplitude envelope) covers a wide frequency range. In many cases the pulse spectrum covers the entire T–S wavelength band. Therefore, using a pulsed-sound approach eliminates the distinction between single-frequency and broadband input.
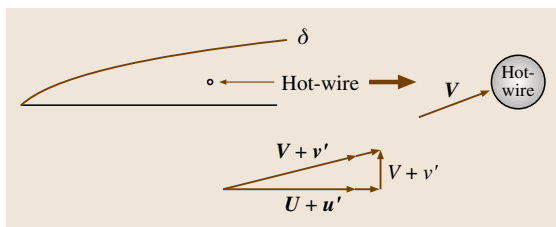

Fig. 12.20 Hot-wire measurements

Hot–Wire Measurements

The hot-wire anemometer is the accepted technique for the measurement of fluctuating velocities $O(10^{-3}U_\infty)$ within the boundary layer. Neither LDV nor PIV have the low-level resolution required for these measurements. Hot wires can accurately measure the streamwise and spanwise velocities (u', w') with the use of straight-wire and slant-wire pairs. Because laminar boundary layers are so thin ($\delta \approx 3$–5 mm), it is not possible to measure v' due to the span of the wire.

If the temperature of the wind tunnel undergoes changes of more than a few degrees between calibrations, temperature compensation must be used. This can be done with a simple computer solution that does both velocity and temperature compensation [12.115].

To do this, one must understand how and what data are retrieved from a hot wire. In a real boundary layer, a hot wire measures the component of velocity perpendicular to the wire as shown in Fig. 12.20.

Although the velocity is 2-D, the output signal is only a combination of U and u' because the vector sum of $U +$
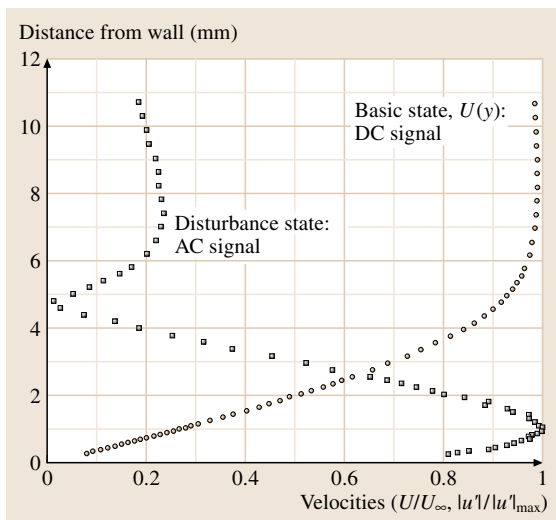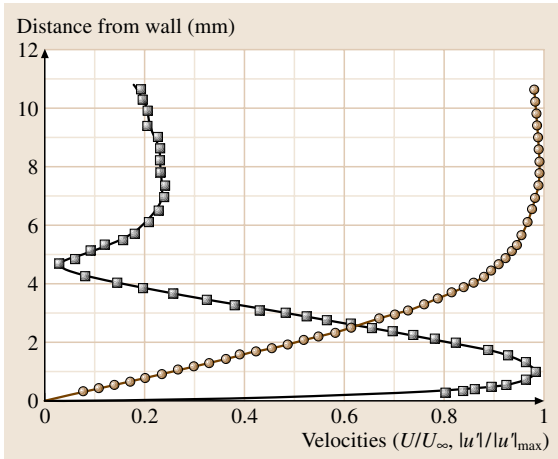

Fig. 12.21 Disturbance and basic-state profiles

Fig. 12.22 Theory and experiment of Blasius velocity profile and T–S amplitude (after [12.94])

Fig. 12.23 Hot-wire measurements near the wall

V is approximately U since $V = O(1/R)$. Similarly, the AC component measures u' and not v' because u' is superposed on U. As a result, the measurement from a hot wire is u'_{rms}, which is proportional to $|D\phi|$ from the OSE. It is straightforward to separate the DC and AC signals.

When attempting to compare with theory, one commonly sees solutions of the OSE displayed in terms of the real and imaginary parts of $\phi(y)$. Since ϕ can be multiplied by any complex number, this is neither revealing nor unique. It is more meaningful to show amplitude, $|\phi|$, and phase, $\psi = \arctan(\phi_i/\phi_r)$. Using the acquired u'_{rms} data, a more-rigorous representation of results is to then plot y as a function of $|D\phi|$, where $|D\phi|$ is a positive real quantity. The resulting plot will look similar to the disturbance state in Fig. 12.21.

Once measurements are processed, they should be correlated with theory. An example with a reduced set of experimental points is shown in Fig. 12.22 [12.94].

To achieve such accuracy, a precision lead screw with anti-backlash bushings should be used in the wall normal direction. One should have the capability to make 100 measurements within the boundary layer which means step sizes on the order of 25 μm.

Wall Effects

In measuring $U(y)$ and $u'(y)$, one will need to find the wall. As the hot wire gets closer to the wall, radiation from the model removes heat from the hot wire, resulting in readings of higher velocity than is actually present. This is shown in Fig. 12.23. To compensate for this effect, stop measurements at $u/U_\infty \approx 0.1$ and for mean flow, use linear extrapolation to the wall.
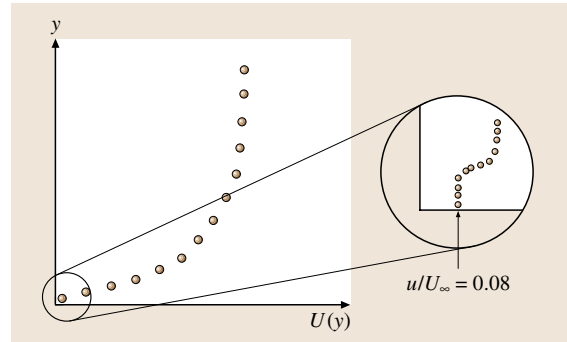
Traverse Blockage

The traverse mechanism may be too large or too close to the hot wire. Moreover, a multi-wire rake may have too much local blockage. What could happen in these cases is that the weak pressure field around the probe support, although unseen in a basic-state measurement, can strongly influence T–S wave amplitude. This can be diagnosed by fixing a very small hot wire to the plate (Fig. 12.24) at a wall-normal location where say, $U/U_\infty \approx 0.3$. Establish the amplitude of a controlled T–S wave as measured by the fixed wire. Move a traverse mounted hot wire to the same location very close to the fixed wire and see if the T–S amplitude on the fixed wire has changed. This is the most sensitive and the only means for determining whether one has eliminated traverse and probe-support interference problems. One should be aware of the fact that traverses and probe supports that are quite suitable for turbulent boundary layers may not be suitable for laminar stability work.

Hot–Film Measurements

The development and application of microthin hot films [12.116, 117] have advanced their use for stability and transition measurements. These films are in the form
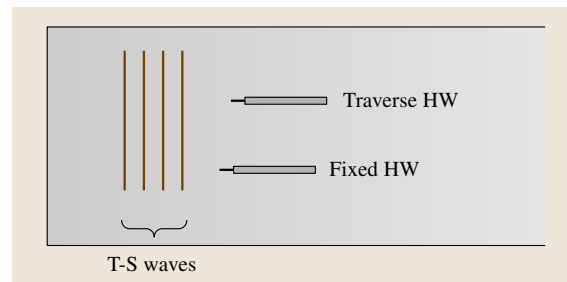

Fig. 12.24 Fixed and traverse hot-wire measurements of T–S waves

of vacuum deposited circuitry on a Kapton sheet. As many as 50 sensors can be concentrated in a small area and can be oriented in any direction. Although difficult to obtain an absolute calibration (one could use a Preston tube over the sensors), this technique is very valuable for measuring wall shear stress fluctuations. Disturbance spectra and transition location can be determined. With the use of multiple hot films, phase and group velocity directions can be determined [12.118]. The use of hot film sheets are superior to individual hot film sensors in that they provide a minimum of disturbance to the flow, are robust, and are easy to apply. This is also a superior technique for flight experiments where it may not be possible to use hot wires. In their simplest, uncalibrated use, an array of sensors would indicate an order of magnitude increase in RMS fluctuations wherever transition to turbulence occurred.

12.3.7 Visualization Methods

Visualization techniques are useful for qualitative information regarding scales and approximate transition location. For stability and transition work, they must always be supported by hot-wire or hot-film measurements.

Smoke–Wire Technique

Most smoke wires used for flow visualization have diameters in the range of $50-80\,\mu m$. This technique was modernized by *Corke* et al. [12.119]. The oil coating (toy train *smoke*) distributes itself periodically along the span of the wire and when the wire is heated it generates a short burst of smoke streaks. The computer initiates the wire voltage and the time-delayed shutter release. When used in stability experiments the smoke wire is placed near the critical layer. Much of the interesting detail is lost if the wire strays from the critical layer. The wake of the smoke wire causes a kink in the basic-state profile which alters its stability characteristics. As a result, if

one examined the amplitude growth of a T–S wave in the stream direction, one would observe an almost step-like increase in amplitude downstream of the smoke wire. The amplitude could easily change by a factor of three due to the smoke wire. Thus, in contrast to its universal use in turbulent boundary layers, special care must be exercised with laminar stability.

One should always be reminded that streaklines do not correspond to streamlines in an unsteady flow. The appearance of a 3-D structure in a streakline is a historical event that is a result of the integration of the history of the smoke. A direct measurement at the location of an apparent 3-D structure may reveal something different. In the same way, visualization should always be accompanied by direct measurements. This type of visualization is good for giving scales over which you need to do the other measurements. An example of the usefulness of the smoke-wire technique is found in *Saric* [12.120].

Surface Coatings

Surface coatings have the ability to determine the approximate location of transition and only rarely something else. The author has tried them all. Shear-sensitive liquid crystals are robust but seem more useful for detecting separation than transition [12.121]. This technique is difficult to apply and introduces a non-trivial surface roughness which affects the stability characteristics. Temperature-sensitive paint (TSP) and pressure-sensitive paint (PSP) have been used for transition detection. PSP and TSP require some application skills and perhaps are best used for complicated shapes. Infrared thermography (IRT) is a non-obtrusive, successful technique requiring a sizable investment in IR cameras (see [12.122] and [12.123] for details). The author has had a great deal of success using naphthalene coatings [12.116,124,125] but health physics issues have arisen regarding the use of naphthalene, trichlorotrifluoroethane, trichloroethane, and other chemicals. For this reason, the author is reluctant to suggest their use.

12.4 Measurements Considerations in Non–Canonical Flows

Wall-bounded turbulent flows are found in a vast number of practical applications, and accordingly have been the focus of research for many years. Most studies have been on the canonical case, that is, a flat-plate turbulent boundary layer developing in a zero pressure gradient. However, most practical boundary layer flows are non-canonical, involving an increased degree of com-

plexity. Some examples include, flow over a skewed or non-axisymmetric geometry, a boundary layer flow encountering an obstacle, or flows involving corners and junctions. In these cases, strong secondary flow and pressure gradients are often present, as is flow separation. Measurements in such flows pose particular challenges compared to the canonical boundary layer flow case, and

this is the topic of this section. The discussion is limited to incompressible boundary layers that may have three-dimensionality in the mean, pressure gradients, or flows that are undergoing mild or incipient separation. In such flows the important feature of the measurement technique is that it must be able to determine the primary flow direction, as well as potentially deal with very high levels of turbulence intensity and/or instantaneous flow reversals. In these cases, perhaps more than others, the measurements must not disturb the flow.

Figure 12.25 shows sketches of typical mean velocity profiles that are being considered. Figure 12.25a corresponds to a boundary layer developing in the presence of three-dimensional pressure gradients. Pressure-driven flows are characterized by free-stream streamlines that curve. The slower fluid near the surface has less inertia than the free-stream fluid and so is turned through a larger angle, as shown in the figure. Such flows may be caused by external geometry changes in those directions or by streamline curvature of the solid body. Three-dimensional turbulent boundary layers may also be formed by shearing. An example would be an initially two-dimensional boundary layer that encounters a section of the wall that is moving at an angle different with respect to that of the free-stream direction. A review of a number of experiments describing how three-dimensionality affects the turbulent boundary layer structure is given by *Eaton* [12.126]. The second type of non-canonical turbulent boundary layers being considered, represented by Fig. 12.25b, are flows that may remain two-dimensional in the mean but involve strong streamwise pressure gradients. In the case of adverse pressure gradients this may lead to flow separation. A good review of turbulent boundary layer flows with separation is given by *Simpson* [12.127].

12.4.1 Pressure Probe Measurements

The standard method for measuring mean or average velocity is to use a Pitot static tube, as described in Sect. 5.1. Accurate use of this probe relies on aligning the probe to a known primary flow direction. *Chue* [12.128] and *Bryer* and *Pankhurst* [12.129] provide a good summary of the accuracy penalties incurred for misalignment for different Pitot-static tube designs. For complex flows, both the dynamic and static pressures are required as well as flow direction. This is most commonly achieved by using combination or multi-hole pressure probes [12.128], which typically require calibration in known flow conditions representative of those in which they will be used.
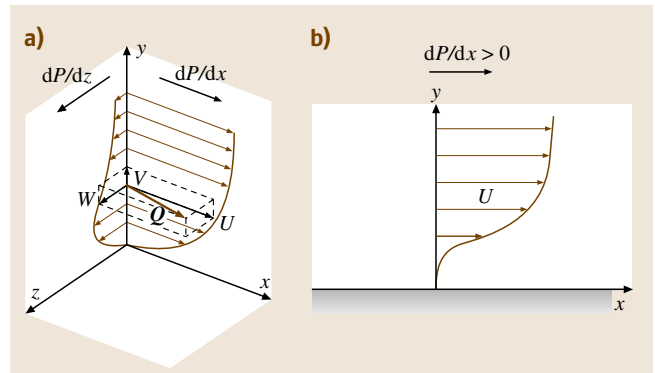

Fig. 12.25a,b Examples of non-canonical boundary layer mean velocity profiles: (**a**) pressure-driven three-dimensional boundary layer, (**b**) adverse-pressure-gradient flow with incipient separation

Many different types of probes have been proposed in the past, either for measuring flow direction, flow speed or both. Figure 12.26 shows sketches of two such devices. Figure 12.26a shows a five-hole probe, which is an example of a multi-hole probe where several small diameter tubes are axisymmetrically arranged around a central total-head tube. The outer tubes have faces that are slanted at a fixed angle as shown in the figure. Figure 12.26b shows a seven-hole probe consisting of a hemispherical tip with one central hole with the remaining holes axisymmetrically distributed at one outer radial distance from the centerline. The holes extend over the length of the probe and connect internally or by tubing to a manometer. Common alternate designs use tips that are machined to a cone or with faceted faces (*cobra* probe).

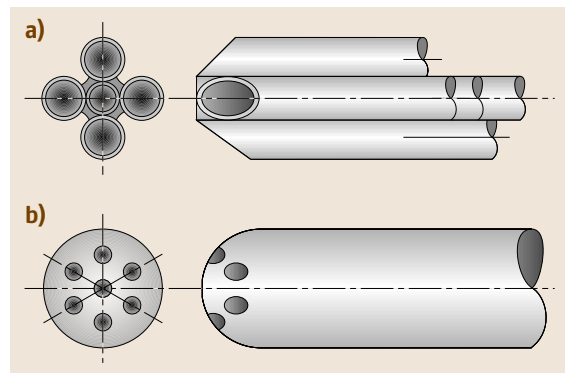Multi-hole pressure probes require calibration, and various schemes have been proposed. See for example

Fig. 12.26 (**a**) Schematic of five-hole probe. (**b**) Seven-hole probe with hemispherical tip

Chue [12.128], *Dominy* and *Hodson* [12.130], *Zilliac* [12.131], *Rediniotis* and *Vijayagopal* [12.132], and *Wenger* and *Devenport* [12.133]. Inaccuracies due to Reynolds-number effects can be significant and need to be considered for accurate measurements. Once calibrated, typical multi-probes have been used in flows where the primary flow direction falls within a cone with an apex angle of up to nominally 75 degrees.

Extended ranges of application, where the approximate primary flow is not known beforehand or where the flow is reversed, have been proposed. However, these usually rely on exhaustive calibrations. *Pisasale* and *Ahmed* [12.134] describe a preprocessing scheme to deal with reverse flows. *Rediniotis* and *Kinser* [12.135] describe an *omnidirectional* pressure probe that consists of a spherical tip with 18 pressure ports. The calibration database that they use is based on readings from 10 000 individual probe orientations in a steady state environment. The time average of the fluctuating pressures in a turbulent flow, when processed with the time-steady calibration information, may not accurately reflect the time-averaged flow field.

For measurements in non-canonical turbulent boundary layers, early studies (before the mid to the late 1970s) used pressure probes extensively, as reviewed by *Vagt* [12.136, 137]. After which, hot wires and LDA became the preferred methods. One of the main concerns about multi-hole probes is their relative large size, and hence their intrusive influence on the flow, particularly for near-wall measurements. This is especially a concern in pressure-driven boundary layers where the imposed pressure field drives the flow. If the pressure probe and associated stems and holders are too large, then the resulting deflected streamlines may manifest in an altered pressure field and hence different flow. In an attempt to overcome these problems, some efforts have gone towards developing miniature probes, such as that of *Ligrani* et al. [12.138]. *Pompeo* et al. [12.139] used a series of pressure probes, including five-hole probes to measure mean flow profiles in a laterally strained turbulent boundary layer. *Westphal* et al. [12.140] developed a single-hole probe in which a single tube cut at 45° is rotated about its axis by a miniature stepper motor. This allows velocity magnitude and angle measurements with a significantly smaller probe, although the measurement procedure is more time-consuming.

When using multi-hole probes, one issue which should always be kept in mind is that the ultimate accuracy of the pressure probe relies on the accuracy of the calibration. Moreover, one uncertainty that remains with most existing calibration techniques is that the calibrations are performed at steady pitch and yaw angles in uniform flows, and no account of the nonlinear effects of the turbulent flow are accounted for. The level of this uncertainty remains unclear.

12.4.2 Turbulence Measurements

The hot-wire and laser Doppler anemometer (LDA) remain the methods of choice for single-point measurements of turbulence quantities, especially if time-series data are required. Comprehensive descriptions of hot-wires and LDA methods are considered in Sect. 5.2 and Sect. 5.3.1 of this handbook, respectively. Here, discussion is limited to considerations specific to the use of these techniques in non-canonical boundary layer flows.

Laser Doppler Anemometry (LDA)

LDA is well suited for non-intrusive measurements of complex flows. A three-component system with frequency shifting can, with reasonable accuracy, measure all three orthogonal components of velocity in complex flows, including regions of separated reversed flow. Successfully implementing a three component system can be difficult, not to mention expensive. Optical access issues quite often limit the type of measurement that can be made. Very-near-wall measurements are particularly challenging because of reflections and/or refraction of the laser beams due to the close proximity of the wall. Even so, successful three-component LDA measurements in three-dimensional boundary layers have been made, see for example the studies of *Driver* and *Hebbar* [12.141], and *Flack* and *Johnston* [12.142, 143].

Perhaps the most accurate LDA measurements to date for the near-wall region of a turbulent boundary layer were made by *DeGraaff* and *Eaton* [12.144]. For those experiments a high-resolution two-component system, with side-scatter collection optics, was custom built giving a measurement volume of 35 μm in diameter, and 60 μm in length. Such small measurement volumes are essential if one wishes to adequately resolve all the near-wall energy-containing motions in most turbulent boundary layers. For example, accurate measurement of Reynolds stresses requires the measurement volume to have a characteristic length typically less than 20 viscous wall units. This is extremely small for boundary layers in most laboratory-scale facilities at high Reynolds number. Figure 12.27, taken from [12.144], illustrates this point well and shows in physical terms the limitation of large measuring volumes (such as for a regular *X*-wire, or standard LDA) as Reynolds number increases in a laboratory wind tunnel.

Song and *Eaton* [12.145] used the same high-resolution LDA system to make measurements in a boundary layer that experienced strong adverse pressure gradient, separation, reattachment, and downstream redevelopment. A common problem of high-spatial-resolution LDA systems is the low data-sampling rate. Extremely high seeding levels are needed to obtain a sufficient statistical sample in a reasonable time, and it is virtually impossible to obtain high-resolution time-resolved LDA data in air flows.

Lowe and *Simpson* [12.146] have recently reported a three-color three-head optical arrangement and a higher-order processing scheme that allows simultaneous measurement of the three component velocity and the flow acceleration. Other notable studies of non-canonical boundary layer flows include that of *Simpson* et al. [12.127, 147] who made accurate measurements using a two-component system in a separating boundary layer, and made comparisons to hot-wire measurements. LDA measurements have also been extensively used for three-dimensional boundary layers. See for example *Olcmen* and *Simpson* [12.148], *Webster*, *DeGraaff* and *Eaton* [12.149], *Compton* and *Eaton* [12.150], and others as reviewed by *Eaton* [12.126].

Hot−Wire Anemometry

The hot-wire, while needing special consideration in non-canonical flows, still remains the most cost effective and simplest method for measuring turbulence flow statistics. A single wire is especially preferred for measurements in very thin boundary layers, or for measurements very close to the wall. For two-component measurements of velocity, *X*-wires are most often used. Three-wire probes are also commonly available commercially, and allow the measurement of all three components of velocity instantaneously. For these probes the calibration schemes are more complex, and the accuracy of the turbulence statistics are in general not as good as can be obtained using *X*-wires (normal and rotated at 90 degrees). Furthermore, single wires and *X*-wires offer the best opportunity for adequate spatial resolution. Details of three-component hot-wire systems are discussed in *Bruun* [12.151] and Sect. 5.2.

The key to successful use of the hot wire is understanding its limitations, and knowing when a reliable measurement can be made. The biggest problem facing conventional hot wires is flow ambiguity, and/or very high levels of turbulence intensity, and these will be discussed in the following.
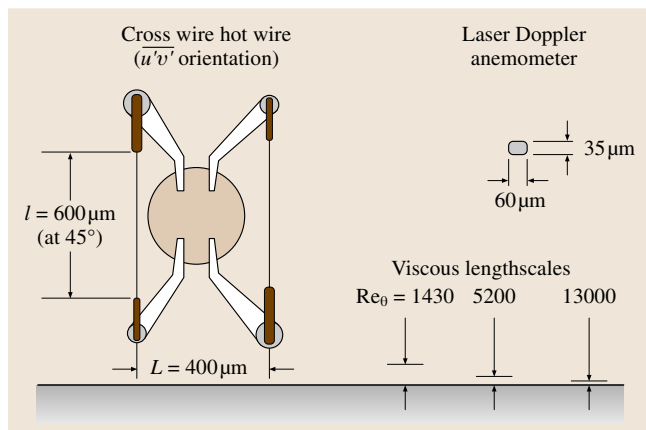

Fig. 12.27 Comparison of typical *X*-wire and required LDA measurement volume for near-wall boundary-layer measurements (after *DeGraaff* and *Eaton* [12.144])

High Turbulence Intensity Flows. For a single wire, the limitations due to large incident velocity vector angles can be understood by considering the response of the wire to an instantaneous flow, as shown in Fig. 12.28a. The long time-averaged velocity is $\overline{U}$, and u, v and w are the turbulent fluctuating components in the Cartesian coordinate system (x, y, z) shown in the figure. The output voltage E from an anemometer may be modeled
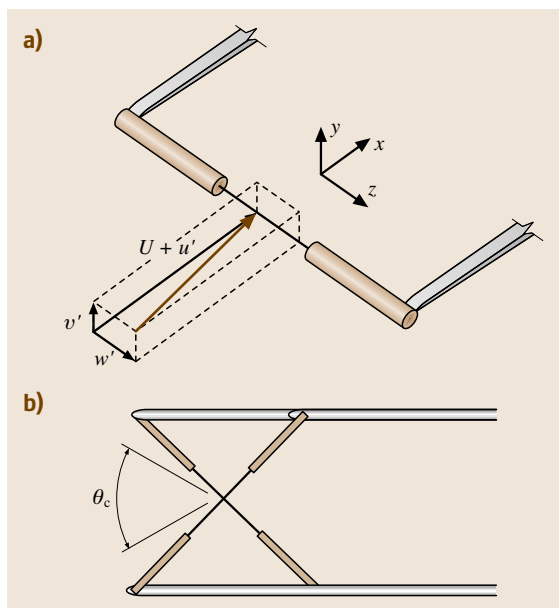

Fig. 12.28 (**a**) Single-normal hot-wire geometry. (**b**) Cone angle θ_c for *X*-wire

using a King's law formulation

$$E^2 = A + BU_e^n \,, \tag{12.37}$$

where U_e is referred to as the effective velocity. A commonly used relationship for U_e is (*Champagne* et al. [12.153, 154])

$$U_e^2 = U_N^2 + k^2 U_L^2 \,, \tag{12.38}$$

where U_N is the velocity normal to the wire, and U_L is the longitudinal component of velocity along the wire. The constant k has a typical value of 0.2. Considering the velocity vector in Fig. 12.28a, and following *Perry* [12.155], the Pythagoras and binomial theorems are used to obtain the expression

$$U_e = (\overline{U} + u) + \frac{\overline{U}}{2}\left[\left(\frac{u}{\overline{U}}\right)^2 + \left(\frac{v}{\overline{U}}\right)^2 + k^2\left(\frac{w}{\overline{U}}\right)^2\right]$$
$$+ \text{higher-order terms} \,. \tag{12.39}$$

Therefore, clearly $u/\overline{U}$, $v/\overline{U}$ and $w/\overline{U}$ need to be small in order to assume

$$U_e \approx \overline{U} + u \,. \tag{12.40}$$

If the turbulence intensities are high, (12.39) may be used to estimate the possible error. *Bruun* [12.151] provides a good list of references of studies documenting uncertainties for flows with very high turbulence intensities. In reverse flows or flows with excessively high turbulence intensity, a way to successfully use a single wire is to *fly* the wire. A *flying hot wire* is a hot-wire device that moves the probe into the primary flow direction with a known bias velocity. The forward bias speed must be sufficiently fast so that the relative $\overline{U}$ is high enough to make the relative $u/\overline{U}$, etc. sufficiently small. *Cantwell* and *Coles* [12.156], *Perry* and *Watmuff* [12.157] and others (*Bruun* [12.151]) have successfully used such an approach in wake flows, and other flows with significant flow reversal. *Perry* and *Li* [12.158] used a flying hot wire in the study of rough-wall boundary layers where high turbulence intensities can also be encountered.

In the case of X-wires, an effective way to qualify the largest acceptable turbulence intensity is to define a *cone angle* [12.159] as shown schematically in Fig. 12.28b. The term cone angle, θ_c, refers to the included angle in the plane of the X-wire of an imaginary cone (assumed to be symmetric) in which the instantaneous velocity vectors fall. *Marusic* and *Perry* [12.152] quantitatively defined the cone angle as

$$\theta_c = 2(|\mu_c| + 3\sigma_c) \,, \tag{12.41}$$

where μ_c and σ_c are the mean and standard deviation, respectively, of the probability distribution function of the measured velocity vector angles. If θ_c exceeds a *critical cone angle* [12.152] then incorrect values of inferred Reynolds stresses will result. Determining the critical cone angle requires an independent method to accurately measure the Reynolds stresses ($\overline{u^2}$, $\overline{v^2}$, $-\overline{uv}$ etc.). *Marusic* and *Perry* [12.152] made measurements in a turbulent boundary layer developing in a strong adverse pressure gradient. They used a flying hot wire to reduce the effective θ_c and compared the measured Reynolds stresses between flying and stationary X-wires. From this, it was determined that for their X-wires ($90°$ included angle) and calibration procedure, the critical cone angle was $40-45°$. Therefore, if a stationary X-wire recorded a θ_c in excess of this value, it was determined to be unreliable. Figure 12.29 is taken from [12.152] and shows the variation of θ_c for stationary and flying hot wires in an adverse-pressure-gradient boundary layer.

The critical cone angle of a X-wire can be increased by either using a special calibration scheme to account for the large incident velocity vector angles, or by using large included angles between the wires. *Skare* and *Krogstad* [12.160] used X-wires with an apex angle of $110°$, and made measurements in a very strong pressure gradient boundary layer flow on the verge of separation. *Elsberry* et al. [12.161] conducted experiments in a boundary layer with incipient separation. They adopted a calibration scheme that extended their effective critical cone angle, and made comparative measurements with LDA to confirm the accuracy of their hot-wire measurements.
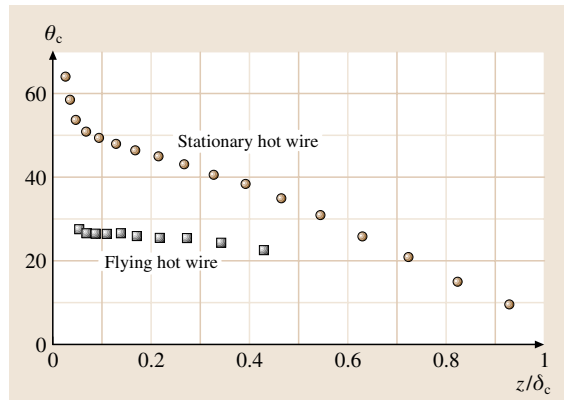

Fig. 12.29 Comparison of cone angle for stationary and flying X-wire across a turbulent boundary with strong adverse pressure gradient (after *Marusic* and *Perry* [12.152])

Unsteady, Reverse Flows. As discussed above, a flying hot wire may be used in reverse flows to remove the directional ambiguity involved. However, in many non-canonical flow applications this is not possible or convenient, due to the mechanical complexity involved with a flying apparatus, and often a continuous time series at a given point in the flow is required. Various thermal anemometry techniques have been developed over the years to address this issue, and many are reviewed by *Bruun* [12.151]. The most prominent of these is the pulsed-wire anemometer originally developed by *Bradbury* and *Castro* [12.163]. A design specific for near-wall flows was developed by *Westphal* et al. [12.162], and is shown in Fig. 12.30. The principal of operation relies on a central wire that is heated in short pulses, and upstream and downstream hot wires that operate effectively as temperature sensors. Typically the central wire is heated periodically, and the velocity is measured from the time of flight of the hot tracer fluid from the central wire to the downstream or upstream wires, giving the forward or reverse velocities respectively. Other pulsed-wire anemometer designs for near-wall flows have been proposed by *Castro* and *Dianat* [12.164] and *Devenport* et al. [12.165] and others. Limitations on the use of these probes is dependent on thermal diffusion considerations as discussed by *Schober* et al. [12.166], and in general the frequency response is limited to tens of Hz.
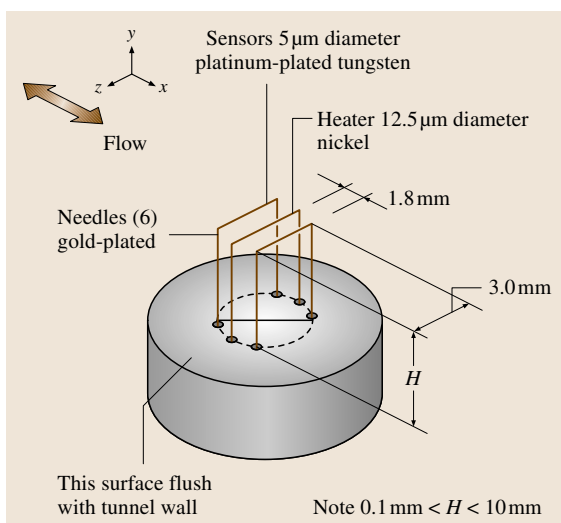

Fig. 12.30 Pulsed wire probe, suitable for measurement of near-wall velocity and wall-shear stress in reverse flows (after *Westphal* et al. [12.162])

12.4.3 Wall Shear Stress

A comprehensive review of different methods for measuring wall shear stress is given in Sect. 12.1. For non-canonical boundary layer flows the number of available techniques is greatly reduced, especially for three-dimensional boundary layers and flows with separated flow regions. For three-dimensional boundary layers, the skin friction measurement technique needs to be able to determine the principal wall shear stress magnitude and direction.

Of the direct methods, the floating element method can in principle be used for complex flows. However, its use is complicated in pressure gradients, where the device needs to be able to account for the pressure gradient contribution to the force balance across the sensor. Also, in incipient separation flows where the wall shear stress is very small, the signal-to-noise ratio is usually prohibitively small. Oil-film interferometry is perhaps the best of the direct methods for steady-state conditions. Most systems now use video cameras to record the interference fringe patterns as a function of time from an oil drop being sheared by the flow. From the two-dimensional images it is usually fairly straightforward to determine the direction of principal wall shear stress.

Of the indirect methods, several methods are available but each has its disadvantages. For example, one method is to use an equivalent of the Clauser chart, where total mean velocity Q at a wall-normal position is measured and assumed to follow a logarithmic law of the wall, thus yielding Q_τ, the total wall shear velocity. This method was used by *Compton* and *Eaton* [12.150] in their pressure-driven three-dimensional boundary layer study. This technique is not regarded as ideal as there is considerable debate as the validity of the law of the wall in complex flows.

For time-resolved wall shear stress measurements in attached flows the most common method is to use a hot wire positioned very close to the wall in the viscous sublayer. The wall shear stress, τ_0, is then known from the measured velocity U from the linear relationship

$$\tau_0 = \frac{\mu}{y} U \, , \tag{12.42}$$

where y is the distance from the wall, and μ is the viscosity of the fluid. For complex flows with flow reversal, pulsed probes such as the one shown in Fig. 12.30 have been used by adopting higher-order similarity formulations ([12.162, 167]). That is, for y small

$$\tau_0 = f(U) \, . \tag{12.43}$$

Part C | 12.4

Other techniques also based on thermal anemometry but with higher-frequency response than pulsed probes have recently been reported. These include the designs by *Spazzini* et al. [12.168] who used two electrically heated hot wires mounted above a cavity, and *Li* and *Naguib* [12.169] who used an oscillating hot-wire technique with a reported frequency response of 1.4 kHz.

12.4.4 Planar and Whole-Field Measurements

The majority of experimental studies on non-canonical turbulent boundary layers to date have been done with single-point measurements. This approach is perhaps still the best if the aim is to measure accurate turbulence statistics. However, often it is desirable to measure the velocity field simultaneously in a plane or volume, and using arrays of single-point probes is far from ideal. Fortunately, over the past decade rapid advances in digital camera and laser technology have seen techniques such as particle image velocimetry (PIV) become much more prolific. Carefully applied, PIV can be an excellent and very useful method for measuring complex boundary layer flows. Some recent studies include: Kiesow and Plesniak [12.170] who made PIV measurements in a shear-driven three-dimensional turbulent boundary layer, and *Angele* [12.171] who made measurements in a separating adverse-pressure-gradient turbulent boundary layer.

A thorough and detailed description of issues relating to PIV and its accurate use is presented in Sect. 5.3.2. For non-canonical turbulent boundary layers, and highly complex flows in general, a number of particular challenges to the accuracy of PIV are worth noting here. PIV is a technique synonymous with compromises – at least when it comes to the choice of parameters. For example, the time delay between consecutive laser sheet pulses needs to be large to minimize the error in the differencing algorithm, but not so large that the light scattering particles have had time to leave the illuminated volume. In highly complex flows, the measurement field

may cover a wide range of velocities and cross-flows, and therefore an optimal choice of measurement parameters, such as laser sheet thickness and time delay between laser pulses, may only apply for a small part of the measurement field. Typically, such errors will show up prominently in measurements of the Reynolds stresses. Another common practical difficulty of using PIV in complex geometries is adequate optical access, both from the standpoint of introducing a laser sheet and taking camera images. One way to overcome this problem is to construct the flow facility out of a transparent material, and use a working fluid with the same optical refractive index as the solid surfaces. Recently, this was successfully achieved by *Uzol* et al. [12.172] in a complex axial turbo-pump flow facility. The authors constructed the rotor, stator and body completely out of transparent acrylic, and used sodium iodide, mixed with water to the right proportion, to match the refractive index of the acrylic.

Several methods exist for the measurement of instantaneous velocity field measurements in a volume, such as holographic techniques. A relatively new technique that is showing promise for whole field measurements in complex boundary layers is four-dimensional (4-D) magnetic resonance velocimetry (4-D MRV) developed by *Elkins* et al. [12.173]. The method is an adaptation of a medical magnetic resonance imaging (MRI) system and provides a non-invasive measurement of three-component mean velocity fields. *Elkins* et al. [12.173] demonstrated the technique in a complex geometry with multiple 180 degree bends. For turbulence measurements in complex geometries, several workers have also proven the effectiveness of holographic PIV. See for example, *Tao*, *Katz* and *Meneveau* [12.174] who made measurements in a turbulent duct flow, and *Konrad*, *Schroder* and *Limberg* [12.175] who made measurements in an internal combustion engine cylinder. Further advances in hologram imaging techniques will likely see the increased use of this method in the future, and possibly for non-canonical turbulent boundary-layer studies.

References

12.1   H. Schlichting, K. Gersten: *Boundary Layer Theory* (Springer, Berlin–Heidelberg 2000)

12.2   H. Tennekes, J. Lumley: *A First Course in Turbulence* (MIT Press, Boston 1972)

12.3   S.B. Pope: *Turbulent Flow* (Cambridge Univ. Press, Cambridge 2000)

12.4   A. Sahay: *The Mean Velocity and the Reynolds Shear Stress in Turbulent Channel and Pipe Flow* (Yale Univ. Press, Cambridge 1997)

12.5   J.C. Klewicki, R.E. Falco: On accurately measuring statistics associated with small scale structure in turbulent boundary layers using

hot-wire probes, J. Fluid Mech. **219**, 119–142 (1990)

12.6 R.D. Moser, J. Kim, N.N. Mansour: Direct numerical simulation of turbulent channel flow up to $R_\tau =$ 590, Phys. Fluids **11**, 943–954 (1999)

12.7 T. Wei, P. Fife, J. Klewicki, P. McMurtry: Properties of the mean momentum balance in turbulent boundary layer, pipe and channel flows, J. Fluid Mech. **522**, 303–327 (2005)

12.8 A.A. Townsend: *The Structure of Turbulent Shear Flow* (Cambridge Univ. Press, Cambridge 1976)

12.9 R.W. Fox, A.T. McDonald: *Introduction to Fluid Mechanics* (Wiley, New York 2000)

12.10 P. Fife, T. Wei, J. Klewicki, P. McMurtry: Stress gradient balance layers and scale hierarchies in wall-bounded turbulent flows, J. Fluid Mech. **532**, 165–189 (2005)

12.11 A.V. Johansson, P.H. Alfredsson: Effects of imperfect spatial resolution on measurements of wall-bounded turbulent shear flows, J. Fluid Mech. **137**, 409–421 (1983)

12.12 P. Ligrani, P. Bradshaw: Spatial resolution and measurement of turbulence in the viscous sublayer using subminiature hot-wire probes, Exp. Fluids **5**, 407–417 (1987)

12.13 D.B. DeGraaff, J.K. Eaton: Reynolds number scaling of the flat plate turbulent boundary layer, J. Fluid Mech. **422**, 319–346 (2000)

12.14 S.-R. Park, J.M. Wallace: The influence of instantaneous velocity gradients on turbulence properties measured with multi-sensor hot-wire probes, Exp. Fluids **16**, 17–26 (1993)

12.15 R.A. Antonia, Y. Zhu, J. Kim: On the measurement of lateral velocity derivatives in turbulent flows, Exp. Fluids **15**, 65–69 (1993)

12.16 A.B. Folz: *An Experimental Study of the Near-Surface Turbulence in the Atmospheric Boundary Layer* (Univ. of Maryland, College Park 1997)

12.17 C.G. Lomas: *Fundamentals of Hot Wire Anemometry* (Cambridge Univ. Press, Cambridge 1986)

12.18 H.-E. Albrecht, N. Damaschke, M. Borys, C. Tropea: *Laser Doppler and Phase Doppler Measurement Techniques* (Springer, Berlin-Heidelberg 2003)

12.19 M. Raffel, C. Willert, J. Kompenhans: *Particle Image Velocimetry: A Practical Guide* (Springer, Berlin-Heidelberg 2001)

12.20 L.H. Tanner, L.G. Blows: A study of the motion of oil films on surfaces in air flow, with application to the measurement of skin friction, J. Phys. E. **9**, 194–202 (1976)

12.21 J.W. Naughton, M. Sheplak: Modern developments in shear-stress measurement, Prog. Aerospace Sci. **38**, 515–570 (2002)

12.22 J.D. Ruedi, H. Nagib, J. Osterlund, P. Monkewitz: Evaluation of three techniques for wall-shear measurements in three-dimensional flows, Expts. Fluids **35**, 389–396 (2003)

12.23 G.G. Zilliac: Further developments of the fringe-imaging skin friction technique, NASA CR-1100425 (NASA, Washington 1996)

12.24 J.L. Brown and J.W. Naughton: The thin-oil-film equation, NASA/TM 1999-208767 (NASA, Washington 1999)

12.25 H.H. Fernholz, G. Janke, M. Schober, P.M. Wagner, D. Warnack: New developments and applications of skin-friction measuring techniques, Meas. Sci. Technol. **7**, 1396–1409 (1996)

12.26 D.J. Monson, H. Higuchi: Skin friction measurement by a dual-laser-beam interferometer technique, AIAA J. **19**, 739–744 (1981)

12.27 J.D. Murphy, R.V. Westphal: The laser interferometer skin-friction meter: a numerical experimental study, J. Phys. E. **19**, 744–751 (1986)

12.28 K.-S. Kim, G.S. Settles: Skin friction measurements by laser interferometry in shock/boundary-layer interactions, AIAA J. **28**, 133–139 (1990)

12.29 J.H. Harotinidis: The measurement of wall shear stress. In: *In: Advances in Fluid Mechanics*, ed. by M. Gad-el-Hak (Springer, Berlin-Heidelber 1989) pp. 229–261

12.30 K. Lien, J. Monty, M.S. Chong, A. Ooi: The entrance length for fully developed turbulent channel flow. In: *Proceedings of the 15th Australasian Fluid Mechanics Conference*, ed. by M. Behnia, W. Lin, G. McBain (University of Sydney, Sydney 2004)

12.31 F.M. White: *Viscous Flow* (McGraw Hill, New York 2002)

12.32 A.V. Boiko, G.R. Grek, A.V. Dovgal, V.V. Kozlov: *The Origin of Turbulence in Near-Wall Flows* (Springer, Berlin-Heidelberg 2002)

12.33 R. Shaw: The influence of hole dimensions on static pressure measurements, J. Fluid Mech. **7**, 550–564 (1960)

12.34 R.E. Franklin, J.M. Wallace: Absolute measurements of static-hole error using flush transducers, J. Fluid Mech. **42**, 33–48 (1970)

12.35 C. Ducruet, A. Dyment: The pressure hole problem, J. Fluid Mech. **142**, 251–267 (1984)

12.36 B.J. McKeon, A.J. Smits: Static pressure correction in high Reynolds number fully developed turbulent pipe flow, Meas. Sci. Tech. **13**, 1608–1614 (2002)

12.37 B.J. McKeon: *High Reynolds Number Turbulent Pipe Flow* (Princeton Univ. Press, Princeton 2003)

12.38 M.J. Walsh: Riblets. In: *In: Viscous Drag Reduction in Boundary Layers*, ed. by D.M. Bushnell, J.N. Hefner (AIAA Progress in Astronautics and Aeronautics, Reston 1989) pp. 203–254

12.39 J.H. Preston: The determination of turbulent skin friction by means of Pitot tubes, J. R. Aeronaut. Soc. **58**, 109–121 (1953)

12.40 V.C. Patel: Calibration of the Preston tube limitation on its use in pressure gradients, J. Fluid Mech. **23**, 185–208 (1965)

12.41 M.R. Head, V.V. Ram: Simplified presentation of Preston tube calibration, Aeronaut. Q. **22**, 295–300 (1971)

12.42 T.J. Hanratty, J.A. Campbell: Measurement of wall shear stress. In: *Fluid Mechanics Measurements*, ed. by R.J. Goldstein (Taylor Francis, 1996)

12.43 T.G. Johansson and L. Castillo: Near-wall measurements in turbulent boundary layers using laser Doppler anemometry, ASME FEDSM2002-31070 (ASME, Metals Park 2002)

12.44 H.M. Nagib and K.A. Chauhan and P.A. Monkewitz: Scaling of high Reynolds number boundary layers revisited, AIAA 2005-4810 (2005)

12.45 F.H. Clauser: Turbulent boundary layers in adverse pressure gradients, J. Aeronaut. Sci. **21**, 91–108 (1954)

12.46 H. Nagib and C. Christophorou and J.-D. Reidi and P. Monkewitz and J. Osterlund and S. Gravante: Can we ever rely on results from wall-bounded turbulent flows without direct measurements of wall shear stress?, AIAA 2004-392 (2004)

12.47 D. Coles: Turbulent Boundary Layers in Pressure Gradients: A Survey Lecture. In: *Proceedings of the 1968 AFOSR-IFP-Stanford Conference on Computation of Turbulent Boundary Layers*, ed. by D. Coles, H. Hirst (Stanford University, Stanford 1969)

12.48 F.S. Sherman: *Viscous Flow* (McGraw-Hill, New York 1990)

12.49 I. Wygnanski, Y. Katz, E. Horev: On the applicability of various scaling laws to the turbulent wall-jet, J. Fluid Mech. **234**, 669–690 (1992)

12.50 A.E. Perry, J.D. Li: Experimental support for the attached-eddy hypothesis in zero-pressure gradient turbulent boundary layers, J. Fluid Mech. **218**, 405–438 (1990)

12.51 D. Coles: The law of the wake in the turbulent boundary layer, J. Fluid Mech. **1**, 191–226 (1956)

12.52 A. Cenedese, G.P. Romano, R.A. Antonia: A comment on the "linear" law of the wall for fully developed turbulent channel flow, Exp. Fluids **25**, 165–170 (1998)

12.53 F. Durst, J. Jovanovic, J. Sender: LDA measurements in the near-wall region of a turbulent pipe flow, J. Fluid Mech. **295**, 305–335 (1995)

12.54 N. Hutchins, K.-S. Choi: Accurate measurements of local skin friction coefficient using hot-wire anemometry, Prog. Aerospace Sci. **38**, 421–446 (2002)

12.55 Y.T. Chew, B.C. Koo, G.L. Li: An investigation of wall effects on hot-wire measurements using a bent sublayer probe, Meas. Sci. Technol. **9**, 67–85 (1994)

12.56 Y.T. Chew, B.C. Koo, G.L. Li: A time-resolved hot-wire shear stress probe for turbulent flow: Use of laminar flow calibration, Exp. Fluids **17**, 75–83 (1994)

12.57 Z. Yue, T.G. Malmstrom: A simple method for low-speed hot-wire anemometer calibration, Meas. Sci. Technol. **9**, 1506–1510 (1998)

12.58 J.M. Allen: Systematic study of error sources in supersonic skin-friction balance measurements, NASA TN D-8291 (1976)

12.59 K.G. Winter: An outline of the techniques available for the measurement of skin friction in turbulent boundary layers, Prog. Aerospace Sci. **18**, 1–57 (1977)

12.60 J.M. Allen: Experimental study of error sources in skin friction balance measurements, J. Fluids Eng. **99**, 197–204 (1977)

12.61 M. Acharya: Development of a floating element for measurement of surface shear stress, AIAA J. **23**, 410–415 (1985)

12.62 D. Frei, H. Thomann: Direct measurements of skin friction in a turbulent boundary layer with strong adverse pressure gradient, J. Fluid Mech. **101**, 79–95 (1980)

12.63 M.A. Schmidt, R.T. Howe, S.D. Senturia, J.H. Haritonidis: Design and calibration of a microfabricated floating-element shear-stress sensor, IEEE Trans. Electron. Dev. **35**, 750–757 (1988)

12.64 L. Lofdahl, M. Gad-el-Hak: MEMS-based pressure and shear stress sensors for turbulent flows, Meas. Sci. Technol. **10**, 665–686 (1999)

12.65 W. Heuer, I. Marusic: Turbulence wall-shear stress sensor for the atmospheric surface layer, Meas. Sci. Technol. **16**, 1644–1649 (2005)

12.66 P.H. Alfredsson, A.V. Johansson, J.H. Haritonidis, H. Eckelmann: The fluctuating wall-shear stress and the velocity field in the viscous sublayer, Phys. Fluids **31**, 1026–1033 (1988)

12.67 V.A. Sanborn: *Resistance Temperature Transducers* (Metrology, Fort Collins 1972)

12.68 K. Collela, W. Keith: Measurements and scaling of wall shear stress fluctuations, Experiments in Fluids **34**, 253–260 (2003)

12.69 A.N. Menendez, B.R. Ramaprian: The use of flush-mounted hot-film gages to measure skin friction in unsteady boundary layers, J. Fluid Mech. **161**, 139–159 (1985)

12.70 D.B. DeGraaff, J.K. Eaton: A high-resolution laser Doppler anemometer: Design, qualification and uncertainty, Exp. Fluids **30**, 522–530 (2000)

12.71 F. Durst, M. Fischer, J. Jovanovic, H. Kikura: Methods to set up and investigate low Reynolds number, fully developed turbulent plane channel flows, J. Fluid Eng. **120**, 496–503 (1998)

12.72 R.B. Hill, J.C. Klewicki: Data reduction methods for flow tagging velocity measurements, Expts. Fluids **20**, 142–151 (1996)

12.73 J.C. Klewicki, R.B. Hill: Spatial structure of negative $\partial u/\partial y$ in a low R_θ turbulent boundary layer, J. Fluid Eng. **120**, 773–785 (1998)

12.74 E.M. Thurlow, J.C. Klewicki: An experimental study of turbulent Poiseuille-Couette flow, Phys. Fluids **12**, 865–875 (2000)

12.75 C.P. Gendrich, M.M. Koochesfahani, D.G. Nocera: Molecular tagging velocimetry and other

novel applications of a new phosphorescent supramolecule, Exp. Fluids **23**, 361–372 (1997)

12.76   M.M. Koochesfahani: Molecular tagging velocimetry: Progress and applications, AIAA paper no. 1999-3786 (1999)

12.77   D.G. Bohl, M.M. Koochesfahani: Molecular tagging velocimetry measurements of axial flow in a concentrated vortex core, Phys. Fluids **16**, 4185–4191 (2004)

12.78   M.V. Morkovin: On the many faces of transition. In: *Viscous Drag Reduction*, ed. by C.S. Wells (Plenum, New York 1969)

12.79   H.L.Reed, W.S. Saric, D. Arnal: Linear Stability Theory Applied to Boundary Layers, Ann. Rev. Fluid Mech. **28**, 389–428 (1996)

12.80   P.G. Drazin: *Introduction to Hydrodynamic Stability* (Cambridge Univ. Press, Cambridge 2002)

12.81   W.O. Criminale, T.L. Jackson, R.D. Joslin: *Theory and Computation in Hydrodynamic Stability* (Cambridge Univ. Press, Cambridge 2003)

12.82   E. Reshotko: Boundary-layer stability and transition, Ann. Rev. Fluid Mech. **8**, 311 (1976)

12.83   E. Reshotko: Boundary layer instability, transition, and control, AIAA 94-0001 (1994)

12.84   E. Reshotko: A Program for Transition Research, AIAA J. **13**, 261–265 (1975)

12.85   G.B. Schubauer, H.K. Skramstad: Laminar boundary-layer oscillations and transition on a flat plate. J. Res. Nat'l. Bur. Stand. 38 (1947) 251

12.86   P.S. Klebanoff, K.D. Tidstrom, L.M. Sargent: The three-dimensional nature of boundary-layer instability, J. Fluid Mech. **12**, 1 (1962)

12.87   W.S. Saric, G.A. Reynolds: Experiments on the nonlinear stability of waves in a boundary layer. In: *Laminar-Turbulent Transition*, Vol. I, ed. by R. Eppler, H. Fasel (Springer, Berlin-Heidelberg 1980)

12.88   N. Lin, H.L. Reed, W.S. Saric: Effect of leading edge geometry on boundary-layer receptivity to freestream sound. In: *Stability, Transition and Turbulence*, ed. by M.Y. Hussaini, A. Kumar, C.L. Street (Springer, New York 1992)

12.89   W.S. Saric, W. Wei, B.K. Rasmussen: Effect of leading edge on sound receptivity. In: *Laminar-Turbulent Transition Vol. IV*, ed. by R. Kobayashi (Proc. IUTAM Symp., Sendai, Japan 1995)

12.90   W.S. Saric, E. White: Influence of High-Amplitude Noise on Boundary-Layer Transition to Turbulence, AIAA 98-2645 (1998)

12.91   T. Herbert: Three-dimensional phenomena in the transitional flat-plate boundary layer, AIAA 85-0489 (1985)

12.92   B.G.B. Klingmann, A.V. Boiko, K.J.A. Westin, V.V. Kozlov, P.H. Alfredsson: Experiments on the stability of Tollmien-Schlichting waves, Eur. J. Mech. B Fluids **12**, 493 (1993)

12.93   F.P. Bertolotti, T. Herbert, P.R. Spalart: Linear and nonlinear stability of the Blasius boundary layer, J. Fluid Mech. **242**, 44 (1992)

12.94   W.S. Saric: Low-speed experiments: Requirements for stability measurements. In: *Instability and Transition*, Vol. I, ed. by Y. Hussaini (Springer, Berlin-Heidelberg 1990) p. 174

12.95   J.A. Ross, F.H. Barnes, J.G. Burns, M.A.S. Ross: The flat plate boundary layer, Part 3 Comparison of theory with experiment, J. Fluid Mech. **43**, 819 (1970)

12.96   B. Müller, H. Bippes: Experimental Study of Instability Modes in a Three-Dimensional Boundary Layer, In Fluid Dynamics of Three-Dimensional Turbulent Shear Flows and Transition, AGARD CP 438 (1988) 13-1 – 13-15

12.97   A.M. Naguib, S.P. Gravante, C.E. Wark: Extraction of turbulent wall-pressure time-series using an optimal filtering scheme, Exp. Fluids **22**, 14–22 (1996)

12.98   W.S. Saric, E. Reshotko: Review of Flow Quality Issues in Wind Tunnel Testing, AIAA 98-2613 (1998)

12.99   W.S. Saric, S. Takagi, M.C. Mousseux: The ASU Unsteady Wind Tunnel and fundamental requirements for freestream turbulence measurements, AIAA 88-0053 (1988)

12.100 J.M. Kendall: Boundary layer receptivity to freestream turbulence, AIAA 90-1504 (1990)

12.101 W.S. Saric, A.S.W. Thomas: Experiments on the subharmonic route to turbulence in boundary layers. In: *Turbulence and Chaotic Phenomena in Fluids*, ed. by T. Tatsumi (North-Holland, Amsterdam 1984)

12.102 T.C. Corke, R.A. Mangano: Resonant growth of three-dimensional modes in transitioning Blasius boundary layers, J. Fluid Mech. **209**, 93 (1989)

12.103 M. Nishioka, S. Iida, Y. Ichikawa: An experimental investigation of the stability of plane Poiseuille flow, J. Fluid Mech. **72**, 731 (1975)

12.104 J.B. Anders, R.F. Blackwelder: Longitudinal Vortices in a Transitioning Boundary Layer. In: *Laminar-Turbulent Transition Vol. I.*, ed. by R. Eppler, H. Fase (Springer, Berlin-Heidelberg 1980)

12.105 B.A. Singer, H.L. Reed, J.H. Ferziger: Effect of streamwise vortices on transition in plane channel flow, Phys. Fluids A **1**, 1960 (1989)

12.106 W.S. Saric, J.A. Hoos, R.H. Radeztsky Jr: Boundary-layer receptivity of sound with roughness. In: *Boundary Layer Stability and Transition FED-Vol. 114*, ed. by D.C. Reda, H.L. Reed, R. Kobayashi (ASME, New York 1991)

12.107 C.F. Knapp, P.J. Roache: A combined visual and hot-wire anemometer investigation of boundary-layer transition, AIAA J. **6**, 29 (1968)

12.108 K.R. Sreenivasan, S. Raghu, B.T. Chu: The control of pressure oscillations in combustion and fluid dynamical systems, AIAA 85-0540 (1985)

12.109 Yu.S. Kachanov, V.Ya. Levchenko: Resonant interactions of disturbances in transition to turbulence in a boundary layer, J. Fluid Mech. **138**, 209 (1984)

12.110 L.M. Mack: Line sources of instability waves in a Blasius boundary layer, AIAA 84-0168 (1984)

12.111 P.T. Pupator, W.S. Saric: Control of Random Disturbances in a Boundary Layer, AIAA 89-1007 (1989)

12.112 R.W. Wlezien and D.E. Parekh and T.C. Island: Measurement of acoustic receptivity at leading edges and porous strips, Appl. Mech. Rev., 43:S167 (1990)

12.113 W.S. Saric, H.L. Reed, E.J. Kerschen: Boundary-Layer Receptivity to Freestream Disturbances, Ann. Rev. Fluid Mech. Vol. **34**, 291–319 (2002)

12.114 E.B. White, W.S. Saric, R.H. Radeztsky Jr: Leading-Edge Acoustic Receptivity Measurements Using a Pulsed-Sound Technique. In: *Laminar-Turbulent Transition*, Vol. V, ed. by W. Saric, H. Fasel (Springer, Berlin-Heidelberg 2000) pp. 103–108

12.115 R.H. Radeztsky Jr., M.S. Reibert, S. Takagi: A software solution to temperature-induced hot-wire voltage drift, Proc. 3rd International Symposium on Thermal Anemometry, ASME-FED (June 1993)

12.116 J.R. Dagenhart, W.S. Saric, M.C. Mousseux, J.P. Stack: Crossflow-vortex instability and transition on a 45-degree swept wing, AIAA 89-1892 (1989)

12.117 S.M. Mangalam, D.V. Maddalon, W.S. Saric, N.K. Agarwal: Measurements of crossflow vortices, attachment-line flow, and transition using microthin hot films, AIAA 90-1636 (1990)

12.118 H. Deyhle, G. Höhler, H. Bippes: Experimental investigation of instability wave-propagation in a 3-D boundary-layer flow, AIAA J. **31**, 637 (1993)

12.119 T.C. Corke, D Koga, R. Drubka, H. Nagib: A new technique for introducing controlled sheets of smoke streaklines in wind tunnels, Proc. Int'l Congress on Instrumentation in Aerospace Simulation Facilities, IEEE Pub. 77 (1974) CH 1250-8, AES

12.120 W.S. Saric: Visualization of different transition mechanisms, Phys. Fluids **29**, 2770 (1986)

12.121 D.C. Reda: Observations of dynamic stall phenomena using liquid crystal coating, AIAA J. **29**, 308 (1991)

12.122 W.S. Saric, H.L. Reed, D.W. Banks: Flight Testing of Laminar Flow Control in High-Speed Boundary Layers, RTO-MP-AVT-111/RSM (2005)

12.123 S. Zuccher, W.S. Saric: Infrared Thermography Investigations in Transitional Supersonic Boundary Layers. Exps. Fluids. In Press (2006)

12.124 R.H. Radeztsky, Jr, M.S. Reibert, W.S. Saric: Development of stationary crossflow vortices on a swept wing, AIAA 94-2374 (1994)

12.125 R.H. Radeztsky, Jr, M.S. Reibert, W.S. Saric, S. Takagi: Effect of micron-sized roughness on transition in swept-wing flows, AIAA 93-0076 (1993)

12.126 J.K. Eaton: Effects of mean flow three dimensionality on turbulent boundary layer structure, AIAA J. **33**, 2020–2025 (1995)

12.127 R.L. Simpson: Turbulent boundary layer separation, Annu. Rev. Fluid Mech. **21**, 205–234 (1989)

12.128 S.H. Chue: Pressure probes for fluid measurements, Prog. Aerospace Sci. **16**, 147–223 (1975)

12.129 D.W. Bryer, R.C. Pankhurst: *Pressure-probe methods for determining wind speed and flow direction* (National Physical Laboratory, Teddington 1971)

12.130 R.G. Dominy, H.P. Hodson: An investigation of factors influencing the calibration of five-hole probes for three-dimensional flow measurements, J. Turbomach. **115**, 513–519 (1993)

12.131 G.G. Zilliac: Modelling, calibration and error analysis of seven-hole pressure probes, Exp. Fluids **14**, 104–120 (1993)

12.132 O.K. Rediniotis, R. Vijayagopal: Miniature multi-hole pressure probes and their neural-network-based calibration, AIAA J. **37**, 666–674 (1999)

12.133 C.W. Wenger, W.J. Devenport: Seven-hole pressure probe calibration method utilizing look-up error tables, AIAA J. **37**, 675–679 (1999)

12.134 A.J. Pisasale, N.A. Ahmed: Examining the effect of flow reversal on seven-hole probe measurements, AIAA J. **41**, 2460–2467 (2003)

12.135 O.K. Rediniotis, R.E. Kinser: Development of a nearly omnidirectional velocity measurement pressure probe, AIAA J. **36**, 1854–1860 (1998)

12.136 J.D. Vagt: Experimental techniques in three-dimensional turbulent boundary layers. In: *IUTAM Symposium: Three-dimensional turbulent boundary layers*, ed. by H.H. Fernholz, E. Krause (Springer, New York 1982)

12.137 H.H. Fernholz and E. Krause: Three-dimensional turbulent boundary layers, IUTAM Symposium, Berlin, (1982)

12.138 P.M. Ligrani, B.A. Singer, L.R. Baun: Miniature five-hole pressure probe for measurements of three mean velocity components in low-speed flows, J. Phy. E: Sci. Instrum. **22**, 868–876 (1989)

12.139 L. Pompeo, M.S.G. Bettelini, H. Thomann: Laterally strained turbulent boundary layers near a plane of symmetry, J. Fluid Mech. **257**, 507–532 (1993)

12.140 R.V. Westphal, M. Prather, and M. Toyooka: Rotatable single hole pressure probe for flow velocity and direction, AIAA-2002-3138 (2002)

12.141 D. Driver, S. Hebbar: Experimental study of a three-dimensional, shear-driven, turbulent boundary layer, AIAA J. **25**, 35–42 (1987)

12.142 K. Flack, J. Johnston: Near-wall flow in a three-dimensional turbulent boundary layer on the endwall of a rectangular bend, ASME Fluids Eng. Div. **184**, 1–19 (1994)

12.143 J. Johnston, K. Flack: Advances in three-dimensional turbulent boundary layers with an emphasis on the wall-layer regions, ASME J. Fluids Eng. **118**, 219–232 (1996)

12.144 D.B. DeGraaff, J.K. Eaton: Reynolds number scaling of the flat plate turbulent boundary layer, J. Fluid Mech. **422**, 319–346 (2000)

12.145 S. Song, J.K. Eaton: Reynolds number effects on a turbulent boundary layer with separation, reattachment, and recovery, Exp. Fluids **36**, 246–258 (2004)

12.146 K.T. Lowe, R.L. Simpson: Measurements of velocity-acceleration statistics in turbulent boundary layers, Int. J. Heat Fluid Flow **27**, 558–565 (2006)

12.147 R.L. Simpson, Y.T. Chew, B.G. Shivaprasad: The structure of a separating turbulent boundary layer. Part 1. Mean flow and Reynolds stresses, J. Fluid Mech. **113**, 23–51 (1981)

12.148 S.M. Olcmen, R.L. Simpson: An experimental study of a three-dimensional pressure-driven turbulent boundary layer, J. Fluid Mech. **290**, 225–262 (1995)

12.149 D.R. Webster, D.B. DeGraaff, J.K. Eaton: Turbulence characteristics of a boundary layer over a swept bump, J. Fluid Mech. **323**, 1–22 (1996)

12.150 D.A. Compton, J.K. Eaton: Near-wall measurements in a three-dimensional turbulent boundary layer, J. Fluid Mech. **350**, 189–208 (1997)

12.151 H.H. Bruun: *Hot-wire Anemometry. Principles and Signal Analysis* (Oxford Univ. Press, Oxford 1995)

12.152 I. Marusic, A.E. Perry: A wall-wake model for the turbulence structure of boundary layers. Part 2. Further experimental support, J. Fluid Mech. **298**, 389–407 (1995)

12.153 F.H. Champagne, C.A. Sleicher, O.H. Wehrmann: Turbulence measurements with inclined hot-wires. Part 1. heat transfer experiments with inclined hot-wire, J. Fluid Mech. **28**, 153–175 (1967)

12.154 F.H. Champagne, C.A. Sleicher: Turbulence measurements with inclined hot-wires. Part 2. hot-wire response equations, J. Fluid Mech. **28**, 177–182 (1967)

12.155 A.E. Perry: *Hot-wire Anemometry* (Clarendon, Oxford 1982)

12.156 B.J. Cantwell, D. Coles: An experimental study of entrainment and transport in the turbulent near wake of a circular cylinder, J. Fluid Mech. **136**, 321–374 (1983)

12.157 A.E. Perry, J.H. Watmuff: The phase-averaged large-scale structures in three-dimensional turbulent wakes, J. Fluid Mech. **103**, 33–51 (1981)

12.158 A.E. Perry, J.D. Li: Experimental support for the attached eddy hypothesis in zero-pressure-gradient turbulent boundary layers, J. Fluid Mech. **218**, 405–438 (1990)

12.159 A.E. Perry, K.L. Lim, S.M. Henbest: An experimental study of the turbulence structure in smooth- and rough-wall boundary layers, J. Fluid Mech. **177**, 437–466 (1987)

12.160 P.E. Skåre, P.-Å. Krogstad: A turbulent boundary layer near separation, J. Fluid Mech. **272**, 319–348 (1994)

12.161 K. Elsberry, J. Loeffler, M.D. Zhou, I. Wygnanski: An experimental study of a boundary layer that is maintained on the verge of separation, J. Fluid Mech. **423**, 227–261 (2000)

12.162 R.V. Westphal, J.K. Eaton, J.P. Johnston: A new probe for measurement of velocity and wall shear stress in unsteady, reversing flow, J. Fluids Eng. **103**, 478–482 (1981)

12.163 L.J.S. Bradbury, I.P. Castro: A pulsed-wire technique for velocity measurements in highly turbulent flows, J. Fluid Mech. **49**, 657–691 (1971)

12.164 I.P. Castro, M. Dianat: Pulsed-wire anemometry near walls, Exp. Fluids **8**, 343–352 (1990)

12.165 W.J. Devenport, G.P. Evans, E.P. Sutton: A traversing pulsed wire probe for measurements near a wall, Exp. Fluids **8**, 336–342 (1990)

12.166 M. Schober, P.E. Hancock, H. Siller: Pulsed-wire anemometry near walls, Exp. Fluids **25**, 151–159 (1998)

12.167 H.H. Fernholz, G. Janke, M. Schober, P.M. Wagner, D. Warnack: New developments and applications of skin-friction measuring techniques, Meas. Sci. Tech. **7**(10), 1396–1409 (1996)

12.168 P.G. Spazzini, G. Iuso, M. Onorato, N. Zurlo: Design, test and validation of a probe for time-resolved measurement of skin friction, Meas. Sci. Tech. **10**, 631–639 (1999)

12.169 Y. Li, A.M. Naguib: High-frequency oscillating hot-wire sensor for near-wall diagnostics in separated flows, AIAA J. **43**(3), 520–529 (2005)

12.170 R.O. Kiesow, M.W. Plesniak: Modification of near-wall turbulence structure in a shear-driven three-dimensional turbulent boundary layer, Exp. Fluids **25**, 233–242 (1998)

12.171 K.P. Angele: Pressure-based scaling in a separating turbulent APG boundary layer, In Proc. ETC9, Southampton, UK, 2002. (ed. I.P. Castro, P.E. Handcock and T.G. Thomas)

12.172 O. Uzol, Y.C. Chow, J. Katz, C. Meneveau: Unobstructed PIV measurements within an axial turbo-pump using liquid and blades with matched refractive indices, Exp. Fluids **33**, 909–919 (2002)

12.173 C.J. Elkins, M. Markl, N. Pelc, J.K. Eaton: 4D magnetic resonance velocimetry for mean velocity measurements in complex turbulent flows, Exp. Fluids **34**, 494–503 (2003)

12.174 B. Tao, J. Katz, C. Meneveau: Geometry and scale relationships in high Reynolds number turbulence determined from three-dimensional holographic velocimetry, Phys. Fluids **12**, 941 (2000)

12.175 R. Konrath, W. Schroder, W. and Limberg: Holographic particle image velocimetry applied to the flow within the cylinder of a four-valve internal combustion engine, Exp. Fluids **33**, 781–793 (2002)

Part C | 12